Plane wave discontinuous Galerkin methods

Master's Thesis

by
Claude Jeffrey Gittelson

supervised by
Prof. Ralf Hiptmair

Department of Mathematics
Eidgenössische Technische Hochschule Zürich
CH-8092 Zurich
Switzerland

January 2008

Abstract

Plane wave discontinuous Galerkin methods for the Helmholtz equation are presented and studied. Numerical experiments analyze their asymptotic convergence behavior as well as their dispersive and dissipative properties. The latter give rise to the pollution effect, which is confirmed computationally. Differences between the ultra-weak variational formulation and other variants of plane wave discontinuous Galerkin methods are highlighted. Also, an approach to adaptively selecting plane wave basis functions is suggested and studied experimentally.

Contents

Chapter 0

Introduction

Standard finite element discretizations of the Helmholtz equation are inefficient at high frequencies. Due to numerical dispersion, the mesh must resolve the wavelength[(i)] to increasing accuracy for large wavenumbers in order to prevent phase errors from building up over the domain and 'polluting' the Galerkin solution, see [7, 15]. This effect is particularly problematic for low order methods. Several techniques have been introduced to improve the accuracy and efficiency of volumetric discretizations for the Helmholtz equation; overviews are given in [24] and [15, Section 4.8].

Many approaches incorporate oscillatory solutions of the homogeneous Helmholtz equation, such as plane waves, into the test and trial space. Partition of unity methods (PUM) use plane waves multiplied by piecewise polynomials as basis functions, [3, 13, 16, 17, 20]. The use of (nonconforming) discontinuous solution spaces allows for plane wave basis functions. In the discontinuous enrichment method (DEM), a polynomial basis is enriched by plane waves within each element, [9, 10, 23]. The ultra-weak variational formulation (UWVF) uses plane wave basis functions with transmitting impedance conditions to weakly enforce continuity between elements, [5, 6, 8, 12, 14]. Other methods are based on least squares [18, 19, 21, 25] or moving least squares [22].

Although often significantly more efficient than standard finite elements, all of these methods come with the handicap of potentially ill-conditioned stiffness matrices (see [5, Section 3.4] for UWVF). In [12], Hiptmair and Perugia introduce a stable basis in a theoretical setting for spaces spanned by plane waves. In the hope that such a basis will become practically applicable, stability and conditioning problems are not emphasized in this paper.

Recently, UWVF was recast as a discontinuous Galerkin (DG) method, [4, 12], facilitating new approaches to its analysis. The analysis in [12] is based on a slightly modified method called the plane wave discontinuous Galerkin (PWDG) method.

This paper studies the PWDG method and UWVF, which can be seen as a special case of PWDG, focussing more on numerical experiments than theoretical analysis. It can be divided into three main parts. The first two chapters present the PWDG method in an abstract setting and go on to discuss details relevant to the choice of parameters and implementation.

[(i)]The wavelength is $\lambda = 2\pi/\omega$, where ω is the wavenumber of the Helmholtz equation.

The PWDG method is defined in Chapter 1. A general derivation of discontinuous Galerkin methods for the Helmholtz equation is given in Section 1.2. This is specialized to plane wave basis functions and PWDG fluxes in Section 1.3. The relationship between PWDG and UWVF is described in Section 1.3.3. Section 1.4 introduces some restrictions to the flux parameters under which the PWDG sesquilinear form becomes coercive. This chapter is based heavily on [12, Sections 1-5].

The author has implemented PWDG in Matlab for two-dimensional problems. Some aspects of this implementation, in particular the approach to computing the entries of the stiffness and mass matrices, are discussed in Chapter 2. Familiarity with standard discontinuous Galerkin methods is assumed and therefore only techniques specific to plane wave basis functions are presented.

The second part of the paper, Chapters 3, 4 and 5, contains a detailed numerical study of the h-convergence behavior of PWDG. Numerical experiments on asymptotic convergence in two dimensions are presented in Chapter 3. Similar experiments can be found in [12, Section 7] and [4, Section 6]; also, relevant convergence theory is presented in [12, Section 5] and [4].

Dispersion and dissipation are studied in Chapter 4. These closely linked concepts are described in a general setting in Section 4.1; numerical results for PWDG in two dimensions are presented in Section 4.2. For large wavenumbers, dispersion and dissipation cause an extra error term, usually only relevant preasymptotically, called the pollution error. This is studied in Chapter 5. By [12, Section 6], pollution only appears in dimensions two and higher for PWDG.

Finally, in Chapter 6, a method is suggested for adaptively selecting plane wave basis functions. A formula is presented for determining propagation directions of new plane wave basis functions given an approximation of the local error. An algorithm based on this formula is defined and studied experimentally; its performance is compared to the spectral version of PWDG with uniform bases.[(ii)]

[(ii)]Note that this approach to an adaptive algorithm is very different from the one presented in [11] for PUM, which is based on h-version finite elements with predetermined dominant propagation directions incorporated into the basis.

Chapter 1

Derivation of plane wave discontinuous Galerkin methods

Plane wave discontinuous Galerkin methods are discontinuous Galerkin methods with plane waves as local basis functions. In this chapter, we derive a general DG method for the Helmholtz equation, specialize to plane wave bases, and define an appropriate class of numerical fluxes. Different choices of flux parameters lead to the ultra-weak variational method or the PWDG methods studied in [12].

1.1   Continuous Problem

Consider the Helmholtz boundary value problem on a bounded Lipschitz domain $\Omega \subset \mathbb{R}^d$ with a constant wavenumber ω and source term $f \in L_2(\Omega)$,

$$-\Delta u - \omega^2 u = f \quad \text{in } \Omega \,, \tag{1.1a}$$
$$u = g^{\mathrm{D}} \quad \text{on } \Gamma^{\mathrm{D}} \,, \tag{1.1b}$$
$$\nabla u \cdot \boldsymbol{n} = g^{\mathrm{N}} \quad \text{on } \Gamma^{\mathrm{N}} \,, \tag{1.1c}$$
$$\nabla u \cdot \boldsymbol{n} + \mathrm{i}\omega u = g^{\mathrm{R}} \quad \text{on } \Gamma^{\mathrm{R}} \,, \tag{1.1d}$$

where, up to a $(d-1)$-dimensional null set, $\partial\Omega$ is the disjoint union of Γ^{D}, Γ^{N} and Γ^{R}, each of which is locally the graph of a Lipschitz function, and g^{D}, g^{N} and g^{R} are in suitable Sobolev spaces on the respective sections of the boundary. We denote by i the imaginary unit and by $\boldsymbol{n}$ the exterior unit normal vector to Ω.

Let g^{D} be extendable to a function $g^{\mathrm{D}} \in H^1(\Omega)$ and denote by $H^1_{\Gamma^{\mathrm{D}}}(\Omega)$ all elements of $H^1(\Omega)$ whose traces vanish in $H^{1/2}(\Gamma^{\mathrm{D}})$. The variational formulation

of (1.1) is to find $\tilde{u} \in H^1_{\Gamma^{\mathrm{D}}}(\Omega)$ such that for all $v \in H^1_{\Gamma^{\mathrm{D}}}(\Omega)$,

$$\int_\Omega \nabla \tilde{u} \cdot \overline{\nabla v}\,\mathrm{d}\boldsymbol{x} - \omega^2 \int_\Omega \tilde{u}\,\overline{v}\,\mathrm{d}\boldsymbol{x} + \mathrm{i}\omega \int_{\Gamma^{\mathrm{R}}} \tilde{u}\,\overline{v}\,\mathrm{d}S = \int_\Omega f\,\overline{v}\,\mathrm{d}\boldsymbol{x}$$
$$- \int_\Omega \nabla g^{\mathrm{D}} \cdot \overline{\nabla v}\,\mathrm{d}\boldsymbol{x} + \omega^2 \int_\Omega g^{\mathrm{D}}\,\overline{v}\,\mathrm{d}\boldsymbol{x} - \mathrm{i}\omega \int_{\Gamma^{\mathrm{R}}} g^{\mathrm{D}}\,\overline{v}\,\mathrm{d}S$$
$$+ \int_{\Gamma^{\mathrm{N}}} g^{\mathrm{N}}\,\overline{v}\,\mathrm{d}S + \int_{\Gamma^{\mathrm{R}}} g^{\mathrm{R}}\,\overline{v}\,\mathrm{d}S \,. \tag{1.2}$$

Definition 1.1. A function $u \in H^1(\Omega)$ is an *exact solution* of (1.1) if $\tilde{u} := u - g^{\mathrm{D}}$ satisfies the variational equation (1.2).

Following [12], we will derive discontinuous Galerkin methods for the Helmholtz equation written as a first-order system. Let

$$\boldsymbol{\sigma} := \frac{1}{\mathrm{i}\omega} \nabla u \,, \tag{1.3}$$

then (1.1) is equivalent to

$$\mathrm{i}\omega\boldsymbol{\sigma} = \nabla u \quad \text{in } \Omega \,, \tag{1.4a}$$
$$-\nabla \cdot \boldsymbol{\sigma} + \mathrm{i}\omega u = \frac{1}{\mathrm{i}\omega} f \quad \text{in } \Omega \,, \tag{1.4b}$$
$$u = g^{\mathrm{D}} \quad \text{on } \Gamma^{\mathrm{D}} \,, \tag{1.4c}$$
$$\mathrm{i}\omega\boldsymbol{\sigma} \cdot \boldsymbol{n} = g^{\mathrm{N}} \quad \text{on } \Gamma^{\mathrm{N}} \,, \tag{1.4d}$$
$$\mathrm{i}\omega\boldsymbol{\sigma} \cdot \boldsymbol{n} + \mathrm{i}\omega u = g^{\mathrm{R}} \quad \text{on } \Gamma^{\mathrm{R}} \,. \tag{1.4e}$$

Let $K \subset \Omega$ be a Lipschitz domain and assume $\boldsymbol{\sigma} \in \boldsymbol{H}(\mathrm{div}; K)$. Then (1.4a) and (1.4b) imply

$$\mathrm{i}\omega \int_K \boldsymbol{\sigma} \cdot \overline{\boldsymbol{\tau}}\,\mathrm{d}\boldsymbol{x} + \int_K u\,\overline{\nabla \cdot \boldsymbol{\tau}}\,\mathrm{d}\boldsymbol{x} - \int_{\partial K} u\,\overline{\boldsymbol{\tau} \cdot \boldsymbol{n}}\,\mathrm{d}S = 0 \quad \forall \boldsymbol{\tau} \in \boldsymbol{H}(\mathrm{div}; K) \,, \tag{1.5a}$$
$$\int_K \boldsymbol{\sigma} \cdot \overline{\nabla v}\,\mathrm{d}\boldsymbol{x} + \mathrm{i}\omega \int_K u\,\overline{v}\,\mathrm{d}\boldsymbol{x} - \int_{\partial K} \boldsymbol{\sigma} \cdot \boldsymbol{n}\,\overline{v}\,\mathrm{d}S = \frac{1}{\mathrm{i}\omega} \int_K f\,\overline{v}\,\mathrm{d}\boldsymbol{x} \quad \forall v \in H^1(K) \,. \tag{1.5b}$$

Conversely, (1.5) implies (1.4a) and (1.4b) in K.

1.2   Derivation of general discontinuous Galerkin method

1.2.1   Preliminaries

Let $\mathcal{T}_h$ denote a partition of Ω into Lipschitz subdomains, and let $\mathcal{F}_h$ be the $(d-1)$-skeleton of $\mathcal{T}_h$[(i)][(ii)]. Define $\mathcal{F}_h^{\mathrm{I}} := \mathcal{F}_h \backslash \partial\Omega$ and $\mathcal{F}_h^{\Gamma} := \partial\Omega \cap \mathcal{F}_h$, and further

---

[(i)]Abusing our notation, we will denote by $\mathcal{F}_h$ both the subset of $\mathbb{R}^d$ and the set of all faces of $\mathcal{T}_h$; furthermore, $E \cap \mathcal{F}_h := \{F \in \mathcal{F}_h \,;\, F \subset E\}$ for $E \subset \Omega$ and analogously for similar variables.

[(ii)]A face is any $(d-1)$-dimensional intersection of (the closures of) either two elements of $\mathcal{T}_h$ or one element of $\mathcal{T}_h$ and $\partial\Omega$.

split the latter into $\mathcal{F}_h^{\mathrm{D}} := \Gamma^{\mathrm{D}} \cap \mathcal{F}_h$, $\mathcal{F}_h^{\mathrm{N}} := \Gamma^{\mathrm{N}} \cap \mathcal{F}_h$ and $\mathcal{F}_h^{\mathrm{R}} := \Gamma^{\mathrm{R}} \cap \mathcal{F}_h$. Of course we assume that each boundary face $F \in \mathcal{F}_h^{\Gamma}$ lies completely within either Γ^{D}, Γ^{N} or Γ^{R}, so that the previous three terms are well-defined.

Also, let ∇_h, $\nabla_h\cdot$ and Δ_h denote the elementwise application of ∇, $\nabla\cdot$ and Δ, respectively.

For arbitrary $s \in \mathbb{R}$, define the broken Sobolev spaces

$$H^s(\mathcal{T}_h') \;\; := \;\; \prod_{K \in \mathcal{T}_h'} H^s(K) , \qquad \mathcal{T}_h' \subset \mathcal{T}_h , \qquad (1.6)$$

$$H^s(\mathcal{F}_h') \;\; := \;\; \prod_{F \in \mathcal{F}_h'} H^s(F) , \qquad \mathcal{F}_h' \subset \mathcal{F}_h . \qquad (1.7)$$

Since elements of $H^{\tilde{s}}(\mathcal{T}_h)$ may be discontinuous across interelement boundaries, the traces are not well-defined in any $H^s(\mathcal{F}_h)$. The traces are multivalued on on interior faces and must therefore be seen as elements of

$$T^s(\mathcal{T}_h) := \prod_{K \in \mathcal{T}_h} H^s(\partial K \cap \mathcal{F}_h) , \qquad T(\mathcal{T}_h) := T^0(\mathcal{T}_h) . \qquad (1.8)$$

As in [2] and elsewhere, we can then define averages $\{\!\{\cdot\}\!\}$ and normal jumps $[\![\cdot]\!]$ to transform the multi-valued traces into single-valued functions. Let $\zeta_j := \zeta|_{\partial K_j}$ and let $\boldsymbol{n}_j$ be the exterior unit normal to the element $K_j \in \mathcal{T}_h$. For arbitrary $n \in \mathbb{N}$, the average is defined as

$$\{\!\{\cdot\}\!\} : (T^s(\mathcal{T}_h))^n \to (H^s(\mathcal{F}_h))^n$$

$$\zeta \mapsto \{\!\{\zeta\}\!\} := \begin{cases} \frac{1}{2}(\zeta_1 + \zeta_2) & \text{on } F = \overline{K_1} \cap \overline{K_2} \in \mathcal{F}_h^{\mathrm{I}} \\ \zeta & \text{on } F \in \mathcal{F}_h^{\Gamma} \end{cases} . \qquad (1.9)$$

For scalar-valued functions, the normal jump is the vector-valued function defined by

$$[\![\cdot]\!] : T^s(\mathcal{T}_h) \to (H^s(\mathcal{F}_h))^d$$

$$v \mapsto [\![v]\!] := \begin{cases} v_1 \boldsymbol{n}_1 + v_2 \boldsymbol{n}_2 & \text{on } F = \overline{K_1} \cap \overline{K_2} \in \mathcal{F}_h^{\mathrm{I}} \\ v\boldsymbol{n} & \text{on } F \in \mathcal{F}_h^{\Gamma} \end{cases} \qquad (1.10)$$

and for $\mathbb{C}^d$-valued functions, the normal jump is the scalar-valued function defined by

$$[\![\cdot]\!] : (T^s(\mathcal{T}_h))^d \to H^s(\mathcal{F}_h)$$

$$\boldsymbol{\tau} \mapsto [\![\boldsymbol{\tau}]\!] := \begin{cases} \boldsymbol{\tau}_1 \cdot \boldsymbol{n}_1 + \boldsymbol{\tau}_2 \cdot \boldsymbol{n}_2 & \text{on } F = \overline{K_1} \cap \overline{K_2} \in \mathcal{F}_h^{\mathrm{I}} \\ \boldsymbol{\tau} \cdot \boldsymbol{n} & \text{on } F \in \mathcal{F}_h^{\Gamma} \end{cases} . \qquad (1.11)$$

Averages and normal jumps applied to elements of $H^s(\mathcal{T}_h)$ will be understood as applied to the traces of these elements.

1.2.2 General numerical fluxes

A key ingredient to the discontinuous Galerkin methods will be approximations to the traces of u and $\boldsymbol{\sigma}$ on $\mathcal{F}_h$ called *numerical fluxes*. These may depend on approximations u_h and $\boldsymbol{\sigma}_h$ of u and $\boldsymbol{\sigma}$ as well as on boundary data.

Let $u_h \in H^2(\mathcal{T}_h)$ and $\boldsymbol{\sigma}_h \in (H^1(\mathcal{T}_h))^d$, and let $g \in L_2(\mathcal{F}_h)$ equal the boundary data on boundary faces and zero on interior faces. For each element $K \in \mathcal{T}_h$, let

$$\widehat{u}_h|_{\partial K}(u_h, \boldsymbol{\sigma}_h, g) = \widehat{u}_h^u|_{\partial K}(u_h) + \widehat{u}_h^{\boldsymbol{\sigma}}|_{\partial K}(\boldsymbol{\sigma}_h) + \widehat{u}_h^g|_{\partial K}(g) , \qquad (1.12a)$$

$$\widehat{\boldsymbol{\sigma}}_h|_{\partial K}(u_h, \boldsymbol{\sigma}_h, g) = \widehat{\boldsymbol{\sigma}}_h^u|_{\partial K}(u_h) + \widehat{\boldsymbol{\sigma}}_h^{\boldsymbol{\sigma}}|_{\partial K}(\boldsymbol{\sigma}_h) + \widehat{\boldsymbol{\sigma}}_h^g|_{\partial K}(g) , \qquad (1.12b)$$

where each element on the right hand side is a continuous linear mapping from the corresponding space listed above into $L_2(\partial K)$ for (1.12a) and into $(L_2(\partial K))^d$ for (1.12b). Then the numerical fluxes are linear maps

$$\widehat{u}_h : \; H^2(\mathcal{T}_h) \times (H^1(\mathcal{T}_h))^d \times L_2(\mathcal{F}_h) \to T(\mathcal{T}_h) \qquad \text{and}$$

$$\widehat{\boldsymbol{\sigma}}_h : \; H^2(\mathcal{T}_h) \times (H^1(\mathcal{T}_h))^d \times L_2(\mathcal{F}_h) \to (T(\mathcal{T}_h))^d$$

defined locally by (1.12). The components of the fluxes extend to $\widehat{u}_h^u$, $\widehat{u}_h^{\boldsymbol{\sigma}}$, etc. analogously.

Definition 1.2. The fluxes $\widehat{u}_h$ and $\widehat{\boldsymbol{\sigma}}_h$ are called *consistent* if

$$\widehat{u}_h\left(v, \frac{1}{\mathrm{i}\omega}\nabla v, g\right) = v|_{\mathcal{F}_h} \qquad \text{and} \qquad \widehat{\boldsymbol{\sigma}}_h\left(v, \frac{1}{\mathrm{i}\omega}\nabla v, g\right) = \frac{1}{\mathrm{i}\omega}\nabla v|_{\mathcal{F}_h} \qquad (1.13)$$

for any smooth function v satisfying the boundary conditions (1.1b), (1.1c) and (1.1d). They are called *conservative* if they are single-valued on $\mathcal{F}_h$.

We will assume that $\widehat{u}_h$ and $\widehat{\boldsymbol{\sigma}}_h$ are consistent, but not necessarily conservative. When u_h, $\boldsymbol{\sigma}_h$ and g are clear from the context, we will abbreviate $\widehat{u}_h := \widehat{u}_h(u_h, \boldsymbol{\sigma}, g)$ and similarly. Also, when we are considering a single element $K \in \mathcal{T}_h$, we will write $\widehat{u}_h$ for the single-valued $\widehat{u}_h|_{\partial K}$ defined in (1.12) and analogously for $\widehat{\boldsymbol{\sigma}}_h$ and the components of $\widehat{u}_h$ and $\widehat{\boldsymbol{\sigma}}_h$.

1.2.3 Local formulation

In this section, we will derive an initial version of the general discontinuous Galerkin method.

Let $\boldsymbol{\Sigma}_h(K) \subset (H^1(K))^d$ and $V_h(K) \subset H^2(K)$ be arbitrary subspaces for all $K \in \mathcal{T}_h$, and let $\boldsymbol{\Sigma}_h := \prod_{K \in \mathcal{T}_h} \boldsymbol{\Sigma}_h(K)$ and $V_h := \prod_{K \in \mathcal{T}_h} V_h(K)$ consist of all functions whose restrictions to each element lie in these subspaces. Together with the choice of fluxes from Section 1.2.2 (and the mesh $\mathcal{T}_h$ itself), the choice of these subspaces completely determines the discontinuous Galerkin method.

An initial formulation of this discontinuous Galerkin method is obtained by requiring (1.5) for all elements $K \in \mathcal{T}_h$, with the Sobolev spaces replaced by their respective subsets and the traces of u and $\boldsymbol{\sigma}$ by the numerical fluxes. Thus, the discrete solutions $u_h \in V_h$ and $\boldsymbol{\sigma}_h \in \boldsymbol{\Sigma}_h$ are defined by the conditions

$$\mathrm{i}\omega \int_K \boldsymbol{\sigma}_h \cdot \overline{\boldsymbol{\tau}_h} \, \mathrm{d}\boldsymbol{x} + \int_K u_h \, \overline{\nabla \cdot \boldsymbol{\tau}_h} \, \mathrm{d}\boldsymbol{x} - \int_{\partial K} \widehat{u}_h \, \overline{\boldsymbol{\tau}_h \cdot \boldsymbol{n}} \, \mathrm{d}S = 0 , \qquad (1.14a)$$

$$\int_K \boldsymbol{\sigma}_h \cdot \overline{\nabla v_h} \, \mathrm{d}\boldsymbol{x} + \mathrm{i}\omega \int_K u_h \, \overline{v_h} \, \mathrm{d}\boldsymbol{x} - \int_{\partial K} \widehat{\boldsymbol{\sigma}}_h \cdot \boldsymbol{n} \, \overline{v_h} \, \mathrm{d}S = \frac{1}{\mathrm{i}\omega} \int_K f \, \overline{v_h} \, \mathrm{d}\boldsymbol{x} , \qquad (1.14b)$$

for all $\boldsymbol{\tau}_h \in \boldsymbol{\Sigma}_h(K)$ and $v_h \in V_h(K)$ and for all $K \in \mathcal{T}_h$.

It will be useful to reformulate (1.14). A partial integration of the second term in (1.14a) leads to

$$\int_K \boldsymbol{\sigma}_h \cdot \overline{\boldsymbol{\tau}_h} \, \mathrm{d}\boldsymbol{x} = \frac{1}{\mathrm{i}\omega} \int_K \nabla u_h \cdot \overline{\boldsymbol{\tau}_h} \, \mathrm{d}\boldsymbol{x} + \frac{1}{\mathrm{i}\omega} \int_{\partial K} (\widehat{u}_h - u_h) \, \overline{\boldsymbol{\tau}_h \cdot \boldsymbol{n}} \, \mathrm{d}S \ . \qquad (1.15)$$

If $\nabla_h V_h \subset \boldsymbol{\Sigma}_h$, we can replace the first term of (1.14b) according to (1.15) with $\boldsymbol{\tau}_h = \nabla v_h$ and obtain the system

$$\mathrm{i}\omega \int_K \boldsymbol{\sigma}_h \cdot \overline{\boldsymbol{\tau}_h} \, \mathrm{d}\boldsymbol{x} - \int_K \nabla u_h \cdot \overline{\boldsymbol{\tau}_h} \, \mathrm{d}\boldsymbol{x} - \int_{\partial K} (\widehat{u}_h - u_h) \, \overline{\boldsymbol{\tau}_h \cdot \boldsymbol{n}} \, \mathrm{d}S = 0 \ , \qquad (1.16a)$$

$$\int_K \nabla u_h \cdot \overline{\nabla v_h} \, \mathrm{d}\boldsymbol{x} - \omega^2 \int_K u_h \, \overline{v_h} \, \mathrm{d}\boldsymbol{x} + \int_{\partial K} (\widehat{u}_h - u_h) \, \overline{\nabla v_h \cdot \boldsymbol{n}} \, \mathrm{d}S$$
$$- \mathrm{i}\omega \int_{\partial K} \widehat{\boldsymbol{\sigma}}_h \cdot \boldsymbol{n} \, \overline{v_h} \, \mathrm{d}S = \int_K f \, \overline{v_h} \, \mathrm{d}\boldsymbol{x} \ , \qquad (1.16b)$$

which is to be satisfied for all $\boldsymbol{\tau}_h \in \boldsymbol{\Sigma}_h(K)$ and $v_h \in V_h(K)$ and for all $K \in \mathcal{T}_h$.

Clearly, (1.16) is equivalent to (1.14) since all the steps in its derivation can be reversed. One of its advantages is that the volume terms in (1.16b) can be expressed as an integral over the boundary ∂K if the elements of $V_h(K)$ satisfy the homogeneous Helmholtz equation. Let $\mathcal{N}_\omega(K)$ be the null space of the Helmholtz operator on K,

$$\mathcal{N}_\omega(K) := \left\{ w \in H^2(K) \, ; \, -\Delta w - \omega^2 w = 0 \right\} \ . \qquad (1.17)$$

If $V_h(K) \subset \mathcal{N}_\omega(K)$, then $(-\Delta u_h - \omega^2 u_h) v_h = 0$ on K and therefore, by partial integration, u_h satisfies

$$\int_K \nabla u_h \cdot \overline{\nabla v_h} \, \mathrm{d}\boldsymbol{x} - \omega^2 \int_K u_h \, \overline{v_h} \, \mathrm{d}\boldsymbol{x} = \int_{\partial K} \nabla u_h \cdot \boldsymbol{n} \, \overline{v_h} \, \mathrm{d}S \quad \forall v_h \in V_h(K) \qquad (1.18)$$

and (1.16b) becomes

$$\int_{\partial K} (\widehat{u}_h - u_h) \, \overline{\nabla v_h \cdot \boldsymbol{n}} \, \mathrm{d}S + \int_{\partial K} (\nabla u_h - \mathrm{i}\omega \widehat{\boldsymbol{\sigma}}_h) \cdot \boldsymbol{n} \, \overline{v_h} \, \mathrm{d}S = \int_K f \, \overline{v_h} \, \mathrm{d}\boldsymbol{x} \ . \qquad (1.19)$$

Note that the bilinear form on the left-hand side of (1.19) consists only of integrals over the boundary of K.

An alternative formula for the left-hand side of (1.16b) is obtained either by integrating by parts or by replacing the first term in (1.14b) using (1.14a) with $\boldsymbol{\tau}_h = \nabla v_h$,

$$\int_K u_h \, \overline{(-\Delta v_h - \omega^2 v_h)} \, \mathrm{d}\boldsymbol{x} + \int_{\partial K} \widehat{u}_h \, \overline{\nabla v_h \cdot \boldsymbol{n}} \, \mathrm{d}S - \mathrm{i}\omega \int_{\partial K} \widehat{\boldsymbol{\sigma}}_h \cdot \boldsymbol{n} \, \overline{v_h} \, \mathrm{d}S = \int_K f \, \overline{v_h} \, \mathrm{d}\boldsymbol{x} \ . \qquad (1.20)$$

Again, the volume terms on the left-hand side vanish if $V_h(K) \subset \mathcal{N}_\omega(K)$. In this case, (1.20) becomes just

$$\int_{\partial K} \widehat{u}_h \, \overline{\nabla v_h \cdot \boldsymbol{n}} \, \mathrm{d}S - \mathrm{i}\omega \int_{\partial K} \widehat{\boldsymbol{\sigma}}_h \cdot \boldsymbol{n} \, \overline{v_h} \, \mathrm{d}S = \int_K f \, \overline{v_h} \, \mathrm{d}\boldsymbol{x} \ . \qquad (1.21)$$

1.2.4 Global formulation with a lifting operator

Our next step is to sum the local variational equations given in Section 1.2.3 over all elements $K \in \mathcal{T}_h$. This will lead to the final version of our general discontinuous Galerkin method.

For convenience, we will use the notation

$$\int_{\mathcal{F}_h'} \cdot := \sum_{F \in \mathcal{F}_h'} \int_F \cdot \qquad (1.22)$$

for any $\mathcal{F}_h' \subset \mathcal{F}_h$.

The following well-known formula describes the transformation of boundary integrals from individual element boundaries to integrals over subsets of $\mathcal{F}_h$.

Lemma 1.3. For $v \in T(\mathcal{T}_h)$ and $\boldsymbol{\tau} \in (T(\mathcal{T}_h))^d$,

$$\sum_{K \in \mathcal{T}_h} \int_{\partial K} v \, \boldsymbol{\tau} \cdot \boldsymbol{n} \, \mathrm{d}S = \int_{\mathcal{F}_h^{\mathrm{I}}} \{\!\{v\}\!\} \, [\![\boldsymbol{\tau}]\!] \, \mathrm{d}S + \int_{\mathcal{F}_h^{\mathrm{I}}} [\![v]\!] \cdot \{\!\{\boldsymbol{\tau}\}\!\} \, \mathrm{d}S + \int_{\mathcal{F}_h^{\Gamma}} v \, \boldsymbol{\tau} \cdot \boldsymbol{n} \, \mathrm{d}S \ . \qquad (1.23)$$

Proof. On the left-hand side, the contribution of an interior face $F = \overline{K_1} \cap \overline{K_2} \in \mathcal{F}_h^{\mathrm{I}}$ is

$$\int_F v_1 \boldsymbol{\tau}_1 \cdot \boldsymbol{n}_1 + v_2 \boldsymbol{\tau}_2 \cdot \boldsymbol{n}_2 \, \mathrm{d}S$$

$$= \int_F \left(\frac{v_1 + v_2}{2} + \frac{v_1 - v_2}{2} \right) \boldsymbol{\tau}_1 \cdot \boldsymbol{n}_1 + \left(\frac{v_2 + v_1}{2} + \frac{v_2 - v_1}{2} \right) \boldsymbol{\tau}_2 \cdot \boldsymbol{n}_2 \, \mathrm{d}S$$

$$= \int_F \left(\frac{v_1 + v_2}{2} \right) (\boldsymbol{\tau}_1 \cdot \boldsymbol{n}_1 + \boldsymbol{\tau}_2 \cdot \boldsymbol{n}_2) \, \mathrm{d}S + \int_F (v_1 - v_2) \boldsymbol{n}_1 \cdot \left(\frac{\boldsymbol{\tau}_1 + \boldsymbol{\tau}_2}{2} \right) \, \mathrm{d}S$$

$$= \int_F \{\!\{v\}\!\} \, [\![\boldsymbol{\tau}]\!] \, \mathrm{d}S + \int_F [\![v]\!] \cdot \{\!\{\boldsymbol{\tau}\}\!\} \, \mathrm{d}S$$

since $\boldsymbol{n}_2 = -\boldsymbol{n}_1$, where $v_i = v|_{K_i}$, $\boldsymbol{\tau}_i = \boldsymbol{\tau}|_{K_i}$ and $\boldsymbol{n}_i$ is the outer unit normal to K_i for $i \in \{1, 2\}$. $\qquad \square$

We will use Lemma 1.3 to rewrite the system of equations (1.16). Equation (1.16b) is equivalent to

$$\int_\Omega \nabla_h u_h \cdot \overline{\nabla_h v_h} \, \mathrm{d}\boldsymbol{x} - \omega^2 \int_\Omega u_h \, \overline{v_h} \, \mathrm{d}\boldsymbol{x} + \int_{\mathcal{F}_h^{\mathrm{I}}} \{\!\{\widehat{u}_h - u_h\}\!\} \, \overline{[\![\nabla_h v_h]\!]} \, \mathrm{d}S$$

$$+ \int_{\mathcal{F}_h^{\mathrm{I}}} [\![\widehat{u}_h - u_h]\!] \cdot \overline{\{\!\{\nabla_h v_h\}\!\}} \, \mathrm{d}S - \mathrm{i}\omega \int_{\mathcal{F}_h^{\mathrm{I}}} \{\!\{\widehat{\boldsymbol{\sigma}}_h\}\!\} \cdot \overline{[\![v_h]\!]} \, \mathrm{d}S - \mathrm{i}\omega \int_{\mathcal{F}_h^{\mathrm{I}}} [\![\widehat{\boldsymbol{\sigma}}_h]\!] \, \overline{\{\!\{v_h\}\!\}} \, \mathrm{d}S$$

$$+ \int_{\mathcal{F}_h^{\Gamma}} (\widehat{u}_h - u_h) \, \overline{\nabla_h v_h \cdot \boldsymbol{n}} \, \mathrm{d}S - \mathrm{i}\omega \int_{\mathcal{F}_h^{\Gamma}} \widehat{\boldsymbol{\sigma}}_h \cdot \boldsymbol{n} \, \overline{v_h} \, \mathrm{d}S = \int_\Omega f \, \overline{v_h} \, \mathrm{d}\boldsymbol{x} \qquad (1.24)$$

for all $v_h \in V_h$ and all $\boldsymbol{\tau}_h \in \boldsymbol{\Sigma}_h$. Alternatively, we can apply Lemma 1.3 to equation (1.20) to get the slightly simpler formulation

$$
\int_\Omega u_h \overline{(-\Delta_h v_h - \omega^2 v_h)} \, \mathrm{d}\boldsymbol{x} + \int_{\mathcal{F}_h^{\mathrm{I}}} \{\!\{\widehat{u}_h\}\!\} \, \overline{[\![\nabla_h v_h]\!]} \, \mathrm{d}S + \int_{\mathcal{F}_h^{\mathrm{I}}} [\![\widehat{u}_h]\!] \cdot \overline{\{\!\{\nabla_h v_h\}\!\}} \, \mathrm{d}S
$$

$$
- \mathrm{i}\omega \int_{\mathcal{F}_h^{\mathrm{I}}} \{\!\{\widehat{\boldsymbol{\sigma}}_h\}\!\} \cdot \overline{[\![v_h]\!]} \, \mathrm{d}S - \mathrm{i}\omega \int_{\mathcal{F}_h^{\mathrm{I}}} [\![\widehat{\boldsymbol{\sigma}}_h]\!] \, \overline{\{\!\{v_h\}\!\}} \, \mathrm{d}S + \int_{\mathcal{F}_h^{\Gamma}} \widehat{u}_h \, \overline{\nabla_h v_h \cdot \boldsymbol{n}} \, \mathrm{d}S
$$

$$
- \mathrm{i}\omega \int_{\mathcal{F}_h^{\Gamma}} \widehat{\boldsymbol{\sigma}}_h \cdot \boldsymbol{n} \, \overline{v_h} \, \mathrm{d}S = \int_\Omega f \, \overline{v_h} \, \mathrm{d}\boldsymbol{x} \, . \quad (1.25)
$$

Let $\mathcal{N}_\omega(\mathcal{T}_h) := \prod_{K \in \mathcal{T}_h} \mathcal{N}_\omega(K)$ be the space of functions whose restrictions to each element of the mesh lie in the kernel of the Helmholtz operator, that is,

$$
\mathcal{N}_\omega(\mathcal{T}_h) = \left\{ w \in H^2(\mathcal{T}_h) \, ; \, -\Delta_h w - \omega^2 w = 0 \right\} \, . \quad (1.26)
$$

We saw in Section 1.2.3 that the volume terms in equation (1.16b) can be replaced by integrals over faces if $V_h \subset \mathcal{N}_\omega(\mathcal{T}_h)$. In this case, (1.25) becomes

$$
\int_{\mathcal{F}_h^{\mathrm{I}}} \{\!\{\widehat{u}_h\}\!\} \, \overline{[\![\nabla_h v_h]\!]} \, \mathrm{d}S + \int_{\mathcal{F}_h^{\mathrm{I}}} [\![\widehat{u}_h]\!] \cdot \overline{\{\!\{\nabla_h v_h\}\!\}} \, \mathrm{d}S - \mathrm{i}\omega \int_{\mathcal{F}_h^{\mathrm{I}}} \{\!\{\widehat{\boldsymbol{\sigma}}_h\}\!\} \cdot \overline{[\![v_h]\!]} \, \mathrm{d}S
$$

$$
- \mathrm{i}\omega \int_{\mathcal{F}_h^{\mathrm{I}}} [\![\widehat{\boldsymbol{\sigma}}_h]\!] \, \overline{\{\!\{v_h\}\!\}} \, \mathrm{d}S + \int_{\mathcal{F}_h^{\Gamma}} \widehat{u}_h \, \overline{\nabla_h v_h \cdot \boldsymbol{n}} \, \mathrm{d}S - \mathrm{i}\omega \int_{\mathcal{F}_h^{\Gamma}} \widehat{\boldsymbol{\sigma}}_h \cdot \boldsymbol{n} \, \overline{v_h} \, \mathrm{d}S
$$

$$
= \int_\Omega f \, \overline{v_h} \, \mathrm{d}\boldsymbol{x} \, . \quad (1.27)
$$

Next, consider equation (1.16a). Summing over all elements $K \in \mathcal{T}_h$ with Lemma 1.3 leads to

$$
\mathrm{i}\omega \int_\Omega \boldsymbol{\sigma}_h \cdot \overline{\boldsymbol{\tau}_h} \, \mathrm{d}\boldsymbol{x} - \int_\Omega \nabla_h u_h \cdot \overline{\boldsymbol{\tau}_h} \, \mathrm{d}\boldsymbol{x} - \int_{\mathcal{F}_h^{\mathrm{I}}} \{\!\{\widehat{u}_h - u_h\}\!\} \, \overline{[\![\boldsymbol{\tau}_h]\!]} \, \mathrm{d}S
$$

$$
- \int_{\mathcal{F}_h^{\mathrm{I}}} [\![\widehat{u}_h - u_h]\!] \cdot \overline{\{\!\{\boldsymbol{\tau}_h\}\!\}} \, \mathrm{d}S - \int_{\mathcal{F}_h^{\Gamma}} (\widehat{u}_h - u_h) \, \overline{\boldsymbol{\tau}_h \cdot \boldsymbol{n}} \, \mathrm{d}S = 0 \, . \quad (1.28)
$$

We now have a global formulation of the discontinuous Galerkin method equivalent to (1.16).

Definition 1.4. The *mixed formulation* of the general discontinuous Galerkin method for (1.1) consists of finding $u_h \in V_h$ and $\boldsymbol{\sigma}_h \in \boldsymbol{\Sigma}_h$ such that (1.28) is satisfied for all $\boldsymbol{\tau}_h \in \boldsymbol{\Sigma}_h$ and (1.24) (or, equivalently, (1.25)) is satisfied for all $v_h \in V_h$.

However, this is not the final form of our method. We would like to have a variational formulation only for u_h using test functions $v_h \in V_h$. To this end, we will define a lifting operator $\mathcal{L}_h$ to transform the boundary integrals in (1.28)

into a volume integral. We will then be able to express $\boldsymbol{\sigma}_h$ in terms of u_h, and inserting this into equation (1.24) or (1.25) will lead to the final formulation of the method.

Let the linear operator $\mathcal{L}_h : T(\mathcal{T}_h) \to \boldsymbol{\Sigma}_h$ be defined by the condition

$$
\mathrm{i}\omega \int_\Omega \mathcal{L}_h(v) \cdot \overline{\boldsymbol{\tau}_h} \, \mathrm{d}\boldsymbol{x} = \int_{\mathcal{F}_h^{\mathrm{I}}} \{\!\{v\}\!\} \, \overline{[\![\boldsymbol{\tau}_h]\!]} \, \mathrm{d}S + \int_{\mathcal{F}_h^{\mathrm{I}}} [\![v]\!] \cdot \overline{\{\!\{\boldsymbol{\tau}_h\}\!\}} \, \mathrm{d}S + \int_{\mathcal{F}_h^{\Gamma}} v \, \overline{\boldsymbol{\tau}_h \cdot \boldsymbol{n}} \, \mathrm{d}S \quad (1.29)
$$

for all $\boldsymbol{\tau}_h \in \boldsymbol{\Sigma}_h$. Equation (1.28) is equivalent to

$$
\int_\Omega \boldsymbol{\sigma}_h \cdot \overline{\boldsymbol{\tau}_h} \, \mathrm{d}\boldsymbol{x} = \int_\Omega \left(\frac{1}{\mathrm{i}\omega} \nabla_h u_h + \mathcal{L}_h(\widehat{u}_h - u_h) \right) \cdot \overline{\boldsymbol{\tau}_h} \, \mathrm{d}\boldsymbol{x} \qquad \forall \boldsymbol{\tau}_h \in \boldsymbol{\Sigma}_h \, . \quad (1.30)
$$

Therefore,

$$
\begin{aligned}
\boldsymbol{\sigma}_h &= \frac{1}{\mathrm{i}\omega} \nabla_h u_h + \mathcal{L}_h(\widehat{u}_h(u_h, \boldsymbol{\sigma}_h, g) - u_h) \\
&= \nabla_h u_h - \mathcal{L}_h(u_h) + \mathcal{L}_h(\widehat{u}_h^u(u_h)) + \mathcal{L}_h(\widehat{u}_h^{\boldsymbol{\sigma}}(\boldsymbol{\sigma}_h)) + \mathcal{L}_h(\widehat{u}_h^g(g))
\end{aligned}
$$

and, solving for $\boldsymbol{\sigma}_h$,

$$
\boldsymbol{\sigma}_h = (\mathrm{id}_{\boldsymbol{\Sigma}_h} - \mathcal{L}_h \circ \widehat{u}_h^{\boldsymbol{\sigma}})^{-1} \left(\frac{1}{\mathrm{i}\omega} \nabla_h u_h - \mathcal{L}_h(u_h) + \mathcal{L}_h(\widehat{u}_h^u(u_h)) + \mathcal{L}_h(\widehat{u}_h^g(g)) \right) \, .
$$
$$(1.31)$$

Thus the mixed formulation of the discontinuous Galerkin method is equivalent to the following form of the method.

Definition 1.5. The *primal formulation* of the general discontinuous Galerkin method for (1.1) is defined by the variational equation (1.24) or (1.25) or, if $V_h \subset \mathcal{N}_\omega(\mathcal{T}_h)$, (1.27), which is to be satisfied for all $v_h \in V_h$. If the fluxes $\widehat{u}_h$ and $\widehat{\boldsymbol{\sigma}}_h$ depend on $\boldsymbol{\sigma}_h$, then $\boldsymbol{\sigma}_h$ is replaced by the right-hand side of (1.31).

Note that the discrete test and trial spaces V_h and $\boldsymbol{\Sigma}_h$ in Definitions 1.4 and 1.5 are arbitrary up to the condition $\nabla_h V_h \subset \boldsymbol{\Sigma}_h$.

The primal formulation of the discontinuous Galerkin method is more efficient than the mixed formulation if $\widehat{u}_h$ does not depend on $\boldsymbol{\sigma}_h$, since in this case (1.31) can be used to reduce the variational equation on $\boldsymbol{\Sigma}_h \times V_h$ from Definition 1.4 to one on V_h from Definition 1.5. If $\widehat{u}_h$ does depend on $\boldsymbol{\sigma}_h$, the primal method involves solving (1.31) simultaneously to the variational problem on V_h and there is no gain in efficiency compared to the mixed method.

1.3 Definition of PWDG method

1.3.1 Plane wave basis functions

As described in Sections 1.2.3 and 1.2.4, the primal discontinuous Galerkin method can be formulated without volume terms if $V_h \subset \mathcal{N}_\omega(\mathcal{T}_h)$, that is, if the elements of V_h are in the kernel of the Helmholtz operator on each element $K \in \mathcal{T}_h$. We will consider the case where V_h is spanned locally by plane waves.

Let $D = \{\boldsymbol{d}_1, \ldots, \boldsymbol{d}_p\} \subset S^{d-1} \subset \mathbb{R}^d$ be a finite set of vectors with unit length. Also, let $K \in \mathcal{T}_h$ and choose $\boldsymbol{x}_K \in \mathbb{R}^d$. Then, for $\omega > 0$ and

$$e_j(\boldsymbol{x}) := \mathrm{e}^{\mathrm{i}\omega \boldsymbol{d}_j \cdot (\boldsymbol{x} - \boldsymbol{x}_K)} \qquad \boldsymbol{x} \in \overline{K}, \quad j = 1, \ldots, p, \tag{1.32}$$

define

$$PW_\omega^D(K) := \mathrm{span}_{\mathbb{C}}\{e_1, \ldots, e_p\}, \tag{1.33}$$

the space of complex linear combinations of plane waves with wave number ω and propagation directions D, restricted to the element K[(iii)].

Definition 1.6. A *plane wave discontinuous Galerkin* (PWDG) method for the Helmholtz equation is the discontinuous Galerkin method described in Section 1.2.4 (in either mixed or primal form, see Definitions 1.4 and 1.5) with test and trial space V_h defined locally by $V_h(K) = PW_\omega^D(K)$ for some finite $D \subset S^{d-1}$ for every $K \in \mathcal{T}_h$, and $\boldsymbol{\Sigma}_h$ satisfying $\nabla_h V_h \subset \boldsymbol{\Sigma}_h$.

We will use $\boldsymbol{\Sigma}_h = V_h^d$. When D is clear or irrelevant, we will simply write $PW_\omega(K)$ for $PW_\omega^D(K)$.

In the two-dimensional case, we will often consider equispaced propagation directions on $S^1 \subset \mathbb{R}^2$, that is,

$$D = D^{p,\gamma} := \left\{ \begin{pmatrix} \cos\left(\frac{2\pi}{p}(j-1) + \gamma\right) \\ \sin\left(\frac{2\pi}{p}(j-1) + \gamma\right) \end{pmatrix} ; \; j = 1, \ldots, p \right\} \tag{1.34}$$

with $\gamma \in \mathbb{R}$. For the span of plane waves on K with these propagation directions, we will use the notation $PW_\omega^{p,\gamma}(K) := PW_\omega^{D^{p,\gamma}}(K)$.

For small ω, the natural plane wave basis of $PW_\omega(K)$ defined by (1.32) is unstable since all of the basis functions are nearly constant. In [12, Section 4], Hiptmair and Perugia define an alternative basis that remains stable for $\omega \to 0$. We will stick to the plane wave basis and restrict our experiments to relatively large ω.

1.3.2 Definition of fluxes

In [12, Section 4], Hiptmair and Perugia suggest mesh-dependent fluxes $\widehat{u}_h$ and $\widehat{\boldsymbol{\sigma}}_h$ for the Helmholtz equation with Robin and Dirichlet boundary conditions. We will extend this definition to Neumann boundary conditions.

First, for an element $K \in \mathcal{T}_h$, let $h_K := \mathrm{diam}\, K$ be the diameter of K and define the local mesh size function on $\mathcal{F}_h$ by $\mathtt{h}(F) := \min\{h_K \; ; \; F \subset \partial K\}$.

For $\alpha, \beta, \delta : \mathcal{F}_h \to \mathbb{R}$ and $\boldsymbol{\gamma} : \mathcal{F}_h \to \mathbb{R}^d$ satisfying $\alpha > 0$, $\beta \geq 0$ and $0 < \delta < 1$,

---

(iii) Of course, $\boldsymbol{x}_K$ does not have any effect on $PW_\omega^D(K)$; however, it offers some freedom in the implementation of PWDG methods.

we will consider the numerical fluxes $\widehat{u}_h$ and $\widehat{\boldsymbol{\sigma}}_h$ defined by

on $F \in \mathcal{F}_h^{\mathrm{I}}$:

$$\widehat{\boldsymbol{\sigma}}_h = \frac{1}{\mathrm{i}\omega}\{\!\!\{\nabla_h u_h\}\!\!\} - \alpha[\![u_h]\!] - \frac{\gamma}{\mathrm{i}\omega}[\![\nabla_h u_h]\!] \tag{1.35a}$$

$$\widehat{u}_h = \{\!\!\{u_h\}\!\!\} + \boldsymbol{\gamma} \cdot [\![u_h]\!] - \frac{\beta}{\mathrm{i}\omega}[\![\nabla_h u_h]\!],$$

on $F \in \mathcal{F}_h^{\mathrm{D}}$:

$$\widehat{\boldsymbol{\sigma}}_h = \frac{1}{\mathrm{i}\omega}\nabla_h u_h - \alpha\left(u_h - g^{\mathrm{D}}\right)\boldsymbol{n} \tag{1.35b}$$

$$\widehat{u}_h = g^{\mathrm{D}},$$

on $F \in \mathcal{F}_h^{\mathrm{N}}$:

$$\widehat{\boldsymbol{\sigma}}_h = \frac{1}{\mathrm{i}\omega}g^{\mathrm{N}}\boldsymbol{n} \tag{1.35c}$$

$$\widehat{u}_h = u_h - \frac{\beta}{\mathrm{i}\omega}\left(\nabla_h u_h \cdot \boldsymbol{n} - g^{\mathrm{N}}\right),$$

on $F \in \mathcal{F}_h^{\mathrm{R}}$:

$$\widehat{\boldsymbol{\sigma}}_h = \frac{1}{\mathrm{i}\omega}\nabla_h u_h - (1 - \delta)\left(\frac{1}{\mathrm{i}\omega}\nabla_h u_h + u_h\boldsymbol{n} - \frac{1}{\mathrm{i}\omega}g^{\mathrm{R}}\boldsymbol{n}\right) \tag{1.35d}$$

$$\widehat{u}_h = u_h - \delta\left(\frac{1}{\mathrm{i}\omega}\nabla_h u_h \cdot \boldsymbol{n} + u_h - \frac{1}{\mathrm{i}\omega}g^{\mathrm{R}}\right).$$

These fluxes are clearly consistent, since all of the jump terms in (1.35a) vanish for smooth u_h and (1.13) is satisfied on boundary edges if the boundary conditions hold.

We will concentrate on the case

$$\alpha = \frac{\mathtt{a}}{\omega\mathtt{h}} \qquad \text{and} \qquad \boldsymbol{\gamma} = \boldsymbol{0}, \tag{1.36}$$

where $\mathtt{a} > 0$. Further restrictions on the parameters will be made later on.

Note that these fluxes are independent of $\boldsymbol{\sigma}_h$, that is, $\widehat{u}_h^{\boldsymbol{\sigma}} = 0$ and $\widehat{\boldsymbol{\sigma}}_h^{\boldsymbol{\sigma}} = \boldsymbol{0}$. Therefore, the corresponding primal discontinuous Galerkin method is also independent of $\boldsymbol{\sigma}_h$ and there is no need to define a lifting operator. In fact, the variational equation can be simplified since the fluxes are conservative, ie. they are single-valued. The normal jumps $[\![\widehat{u}_h]\!] = \boldsymbol{0}$ and $[\![\widehat{\boldsymbol{\sigma}}_h]\!] = 0$ disappear and the averages are just the function values, $\{\!\!\{\widehat{u}_h\}\!\!\} = \widehat{u}_h$ and $\{\!\!\{\widehat{\boldsymbol{\sigma}}_h\}\!\!\} = \widehat{\boldsymbol{\sigma}}_h$. Then (1.27), the relevant equation for plane wave basis functions, becomes

$$\int_{\mathcal{F}_h^{\mathrm{I}}} \widehat{u}_h\, \overline{[\![\nabla_h v_h]\!]}\, \mathrm{d}S - \mathrm{i}\omega\int_{\mathcal{F}_h^{\mathrm{I}}} \widehat{\boldsymbol{\sigma}}_h \cdot \overline{[\![v_h]\!]}\, \mathrm{d}S + \int_{\mathcal{F}_h^{\Gamma}} \widehat{u}_h\, \overline{\nabla_h v_h \cdot \boldsymbol{n}}\, \mathrm{d}S$$

$$- \mathrm{i}\omega\int_{\mathcal{F}_h^{\Gamma}} \widehat{\boldsymbol{\sigma}}_h \cdot \boldsymbol{n}\, \overline{v_h}\, \mathrm{d}S = \int_{\Omega} f\, \overline{v_h}\, \mathrm{d}\boldsymbol{x}. \tag{1.37}$$

1.3.3 Relation to the ultra-weak variational method

As described in [12, Section 3], the ultra-weak variational method defined in [5] can be seen as a special case of the plane wave discontinuous Galerkin method

with fluxes of the form defined in Section 1.3.2 in the case of Robin boundary conditions.

The ultra-weak variational method can be formulated as (see [5, Equation (1.4)]): find $u_h \in V_h$ such that for all $v_h \in V_h$

$$\sum_{K \in \mathcal{T}_h} \int_{\partial K} (-\nabla u_h \cdot \boldsymbol{n} + \mathrm{i}\omega u_h) \overline{(-\nabla v_h \cdot \boldsymbol{n} + \mathrm{i}\omega v_h)} \, \mathrm{d}S$$

$$- \int_{\mathcal{F}_h^{\mathrm{I}}} (-\nabla u_h^{(1)} \cdot \boldsymbol{n}^{(1)} + \mathrm{i}\omega u_h^{(1)}) \overline{(\nabla v_h^{(2)} \cdot \boldsymbol{n}^{(2)} + \mathrm{i}\omega v_h^{(2)})} \, \mathrm{d}S$$

$$- \int_{\mathcal{F}_h^{\mathrm{I}}} (-\nabla u_h^{(2)} \cdot \boldsymbol{n}^{(2)} + \mathrm{i}\omega u_h^{(2)}) \overline{(\nabla v_h^{(1)} \cdot \boldsymbol{n}^{(1)} + \mathrm{i}\omega v_h^{(1)})} \, \mathrm{d}S$$

$$= -2\mathrm{i}\omega \int_{\Omega} f \overline{v_h} \, \mathrm{d}\boldsymbol{x} + \int_{\mathcal{F}_h^{\Gamma}} g^{\mathrm{R}} \overline{(\nabla v_h \cdot \boldsymbol{n} + \mathrm{i}\omega v_h)} \, \mathrm{d}S \,, \quad (1.38)$$

where V_h is locally spanned by plane waves, as in Section 1.3.1, and the superscripts $\cdot^{(1)}$ and $\cdot^{(2)}$ refer to the values on the two neighboring elements of an interior face. We will show that it is equivalent to the plane wave discontinuous Galerkin method with parameters

$$\alpha = \frac{1}{2} \,, \qquad \beta = \frac{1}{2} \,, \qquad \boldsymbol{\gamma} = \boldsymbol{0} \qquad \text{and} \qquad \delta = \frac{1}{2} \qquad (1.39)$$

in the fluxes defined in (1.35).

Regrouping terms and using the notation $\cdot^{\mathrm{ext}}$ to refer to the value on the opposite side of an interior face, we can rewrite (1.38) as

$$\sum_{K \in \mathcal{T}_h} \int_{\partial K \setminus \partial \Omega} (-\nabla u_h \cdot \boldsymbol{n} - \nabla u_h^{\mathrm{ext}} \cdot \boldsymbol{n}^{\mathrm{ext}} + \mathrm{i}\omega u_h + \mathrm{i}\omega u_h^{\mathrm{ext}}) \overline{\nabla v_h \cdot \boldsymbol{n}} \, \mathrm{d}S$$

$$+ \int_{\partial K \setminus \partial \Omega} (\nabla u_h \cdot \boldsymbol{n} - \nabla u_h^{\mathrm{ext}} \cdot \boldsymbol{n}^{\mathrm{ext}} - \mathrm{i}\omega u_h + \mathrm{i}\omega u_h^{\mathrm{ext}}) \overline{\mathrm{i}\omega v_h} \, \mathrm{d}S$$

$$+ \int_{\partial K \cap \partial \Omega} (-\nabla u_h \cdot \boldsymbol{n} + \mathrm{i}\omega u_h + g^{\mathrm{R}}) \overline{\nabla v_h \cdot \boldsymbol{n}} \, \mathrm{d}S$$

$$+ \int_{\partial K \cap \partial \Omega} (\nabla u_h \cdot \boldsymbol{n} - \mathrm{i}\omega u_h + g^{\mathrm{R}}) \overline{\mathrm{i}\omega v_h} \, \mathrm{d}S = 2\mathrm{i}\omega \int_{\Omega} f \overline{v_h} \, \mathrm{d}\boldsymbol{x} \,. \quad (1.40)$$

Application of Lemma 1.3 leads to the equivalent formulation

$$\int_{\mathcal{F}_h^{\mathrm{I}}} (2\mathrm{i}\omega \{\!\{u_h\}\!\} - [\![\nabla_h u_h]\!]) \overline{[\![\nabla_h v_h]\!]} \, \mathrm{d}S - \mathrm{i}\omega \int_{\mathcal{F}_h^{\mathrm{I}}} (2\{\!\{\nabla_h u_h\}\!\} - \mathrm{i}\omega [\![u_h]\!]) \cdot \overline{[\![v_h]\!]} \, \mathrm{d}S$$

$$+ \int_{\mathcal{F}_h^{\Gamma}} (-\nabla_h u_h \cdot \boldsymbol{n} + \mathrm{i}\omega u_h + g^{\mathrm{R}}) \overline{\nabla_h v_h \cdot \boldsymbol{n}} \, \mathrm{d}S - \mathrm{i}\omega \int_{\mathcal{F}_h^{\Gamma}} (\nabla_h u_h \cdot \boldsymbol{n} - \mathrm{i}\omega u_h + g^{\mathrm{R}}) \overline{v_h} \, \mathrm{d}S$$

$$= 2\mathrm{i}\omega \int_{\Omega} f \overline{v_h} \, \mathrm{d}\boldsymbol{x} \,. \quad (1.41)$$

Equation (1.41) is simply (1.37) multiplied by $2\mathrm{i}\omega$ with the fluxes defined in (1.35) and the flux parameters (1.39). This shows that the ultra-weak variational method is a special case of a plane wave discontinuous Galerkin method.

1.4 Choice of flux parameters

The theoretical analysis given in [12, Section 5] of the plane wave discontinuous Galerkin method is based on the coercivity of a sesquilinear form related to the left-hand side of (1.37). We will analyze this property in the slightly more general case of a combination of Dirichlet, Neumann and Robin boundary conditions instead of just Robin boundary conditions, using the fluxes (1.35) with parameters of the form (1.36). This will lead to further restrictions to the flux parameters.

Consider a plane wave discontinuous Galerkin method with flux parameters of the form (1.35). Define $C_{\mathrm{tinv}} = C_{\mathrm{tinv}}(K) > 0$ on $K \in \mathcal{T}_h$ as the smallest number such that

$$\|v_h\|_{0,\partial K} \le C_{\mathrm{tinv}} h_K^{-1/2} \|v_h\|_{0,K} \qquad \forall v_h \in V_h(K) \,, \qquad (1.42)$$

where $\|\cdot\|_{0,\cdot}$ refers to the L_2-norm. In [12, Theorem 4.7], Hiptmair and Perugia show that C_{tinv} is bounded independently of ω and K for shape-regular triangular meshes in two dimensions and a constant odd number p of equispaced plane wave propagation directions, ie. $V_h(K) = PW_\omega^{p,\gamma}(K)$ for all $K \in \mathcal{T}_h$.

Since gradients of plane waves are again plane waves in each component, (1.42) holds with the same constant for v_h replaced by ∇v_h.

We will need C_{tinv} on faces of the mesh in addition to individual elements, so for $F \in \mathcal{F}_h$ define $\mathsf{C}_{\mathrm{tinv}}(F) := \max \{C_{\mathrm{tinv}}(K) \,;\, F \subset \partial K\}$.

The general form for the variational problem in a primal discontinuous Galerkin method is to find $u_h \in V_h$ such that for all $v_h \in V_h$,

$$a_h(u_h, v_h) - \omega^2 (u_h, v_h)_\Omega = (f, v_h)_\Omega + \gamma_h(v_h) \,, \qquad (1.43)$$

where $a_h(\cdot, \cdot)$ is a sesquilinear form, $(\cdot, \cdot)_\Omega$ refers to the L_2-scalar product on Ω and $\gamma_h(\cdot)$ is an antilinear functional that contains inhomogeneous boundary data. Following [12], we will show that the auxiliary sesquilinear form

$$b_h(u_h, v_h) := a_h(u_h, v_h) + \omega^2 (u_h, v_h)_\Omega \qquad (1.44)$$

is coercive on $V_h \times V_h$ in a mesh-dependent and parameter-dependent DG-norm.

For the plane wave discontinuous Galerkin method under consideration,

$a_h(\cdot, \cdot)$ has the form

$$a_h(u,v) = \int_\Omega \nabla_h u \cdot \overline{\nabla_h v}\,\mathrm{d}\boldsymbol{x} - \int_{\mathcal{F}_h^{\mathrm{I}}} [\![u]\!] \cdot \overline{\{\!\!\{\nabla_h v\}\!\!\}}\,\mathrm{d}S - \int_{\mathcal{F}_h^{\mathrm{I}}} \{\!\!\{\nabla_h u\}\!\!\} \cdot \overline{[\![v]\!]}\,\mathrm{d}S$$

$$- \int_{\mathcal{F}_h^{\mathrm{D}}} u\,\overline{\nabla_h v \cdot \boldsymbol{n}}\,\mathrm{d}S - \int_{\mathcal{F}_h^{\mathrm{D}}} \nabla_h u \cdot \boldsymbol{n}\,\overline{v}\,\mathrm{d}S - \int_{\mathcal{F}_h^{\mathrm{R}}} \delta\,u\,\overline{\nabla_h v \cdot \boldsymbol{n}}\,\mathrm{d}S$$

$$- \int_{\mathcal{F}_h^{\mathrm{R}}} \delta\,\nabla_h u \cdot \boldsymbol{n}\,\overline{v}\,\mathrm{d}S + \mathrm{i}\omega^{-1}\int_{\mathcal{F}_h^{\mathrm{I}}} \beta\,[\![\nabla_h u]\!]\,\overline{[\![\nabla_h v]\!]}\,\mathrm{d}S + \mathrm{i}\int_{\mathcal{F}_h^{\mathrm{I}}} \frac{\mathsf{a}}{\mathsf{h}}\,[\![u]\!] \cdot \overline{[\![v]\!]}\,\mathrm{d}S$$

$$+ \mathrm{i}\int_{\mathcal{F}_h^{\mathrm{D}}} \frac{\mathsf{a}}{\mathsf{h}}\,u\,\overline{v}\,\mathrm{d}S + \mathrm{i}\omega^{-1}\int_{\mathcal{F}_h^{\mathrm{N}}} \beta\,\nabla_h u \cdot \boldsymbol{n}\,\overline{\nabla_h v \cdot \boldsymbol{n}}\,\mathrm{d}S$$

$$+ \mathrm{i}\omega^{-1}\int_{\mathcal{F}_h^{\mathrm{R}}} \delta\,\nabla_h u \cdot \boldsymbol{n}\,\overline{\nabla_h v \cdot \boldsymbol{n}}\,\mathrm{d}S + \mathrm{i}\omega\int_{\mathcal{F}_h^{\mathrm{R}}} (1 - \delta)\,u\,\overline{v}\,\mathrm{d}S\,. \quad (1.45)$$

This is well-defined on $H^2(\Omega) + V_h$.

We also define on $H^2(\Omega) + V_h$ the closely related seminorm

$$|v|_{\mathrm{DG}}^2 := \|\nabla_h v\|_{0,\Omega}^2 + \omega^{-1}\left\|\beta^{1/2}[\![\nabla_h v]\!]\right\|_{0,\mathcal{F}_h^{\mathrm{I}}}^2 + \left\|\mathsf{a}^{1/2}\mathsf{h}^{-1/2}[\![v]\!]\right\|_{0,\mathcal{F}_h^{\mathrm{I}}}^2$$

$$+ \left\|\mathsf{a}^{1/2}\mathsf{h}^{-1/2}v\right\|_{0,\mathcal{F}_h^{\mathrm{D}}}^2 + \omega^{-1}\left\|\beta^{1/2}\nabla_h v \cdot \boldsymbol{n}\right\|_{0,\mathcal{F}_h^{\mathrm{N}}}^2$$

$$+ \omega^{-1}\left\|\delta^{1/2}\nabla_h v \cdot \boldsymbol{n}\right\|_{0,\mathcal{F}_h^{\mathrm{R}}}^2 + \omega\left\|(1 - \delta)^{1/2}v\right\|_{0,\mathcal{F}_h^{\mathrm{R}}}^2 \quad (1.46)$$

as well as the norm $\|v\|_{\mathrm{DG}}^2 := |v|_{\mathrm{DG}}^2 + \omega^2\|v\|_{0,\Omega}^2$. We will determine parameters for which $b_h(\cdot,\cdot)$ is coercive in this norm in the following proposition, which corresponds to [12, Proposition 5.2].

Proposition 1.7. *If the flux parameters satisfy* $\mathsf{a} > \mathsf{C}_{\mathrm{tinv}}^2/2$ *on* $\mathcal{F}_h^{\mathrm{I}}$, $\mathsf{a} > \mathsf{C}_{\mathrm{tinv}}^2$ *on* $\mathcal{F}_h^{\mathrm{D}}$ *and* $0 < \delta < 1/2$, *then there exists a constant* $C_{\mathrm{coer}} > 0$ *only dependent on* C_{tinv}, a *and* δ *such that*

$$|b_h(v_h, v_h)| \geq C_{\mathrm{coer}}\|v_h\|_{\mathrm{DG}}^2 \qquad \forall v_h \in V_h\,. \quad (1.47)$$

In particular, C_{coer} *is not directly dependent on the mesh, on* ω *or on* V_h.

Proof. By (1.44) and (1.45),

$$b_h(v_h, v_h) = \|\nabla_h v_h\|_{0,\Omega}^2 + \omega^2\|v_h\|_{0,\Omega}^2 - 2\,\mathrm{Re}\int_{\mathcal{F}_h^{\mathrm{I}}} [\![v_h]\!] \cdot \overline{\{\!\!\{\nabla_h v_h\}\!\!\}}\,\mathrm{d}S$$

$$- 2\,\mathrm{Re}\int_{\mathcal{F}_h^{\mathrm{D}}} v_h \cdot \overline{\nabla_h v_h \cdot \boldsymbol{n}}\,\mathrm{d}S - 2\,\mathrm{Re}\int_{\mathcal{F}_h^{\mathrm{R}}} \delta\,v_h \cdot \overline{\nabla_h v_h \cdot \boldsymbol{n}}\,\mathrm{d}S + \mathrm{i}\omega^{-1}\left\|\beta^{1/2}[\![\nabla_h v_h]\!]\right\|_{0,\mathcal{F}_h^{\mathrm{I}}}^2$$

$$+ \mathrm{i}\left\|\mathsf{a}^{1/2}\mathsf{h}^{-1/2}[\![v_h]\!]\right\|_{0,\mathcal{F}_h^{\mathrm{I}}}^2 + \mathrm{i}\left\|\mathsf{a}^{1/2}\mathsf{h}^{-1/2}v_h\right\|_{0,\mathcal{F}_h^{\mathrm{D}}}^2 + \mathrm{i}\omega^{-1}\left\|\beta^{1/2}\nabla_h v_h \cdot \boldsymbol{n}\right\|_{0,\mathcal{F}_h^{\mathrm{N}}}^2$$

$$+ \mathrm{i}\omega^{-1}\left\|\delta^{1/2}\nabla_h v_h \cdot \boldsymbol{n}\right\|_{0,\mathcal{F}_h^{\mathrm{R}}}^2 + \mathrm{i}\omega\left\|(1 - \delta)^{1/2}v_h\right\|_{0,\mathcal{F}_h^{\mathrm{R}}}^2\,. \quad (1.48a)$$

For any $\tilde{\mathcal{F}}_h \subset \mathcal{F}_h$, Young's inequality implies that for arbitrary $\chi = \chi_F > 0$ on every $F \in \tilde{\mathcal{F}}_h$,

$$-2\,\mathrm{Re}\int_{\tilde{\mathcal{F}}_h} [\![v_h]\!] \cdot \overline{\{\!\!\{\nabla_h v_h\}\!\!\}}\,\mathrm{d}S \geq -\left\|\chi^{-1/2}[\![v_h]\!]\right\|_{0,\tilde{\mathcal{F}}_h}^2 - \left\|\chi^{1/2}\{\!\!\{\nabla_h v_h\}\!\!\}\right\|_{0,\tilde{\mathcal{F}}_h}^2\,. \quad (1.48b)$$

We will use (1.42) to estimate the second term further. Let $\tilde{\mathcal{F}}_h = \tilde{\mathcal{F}}_h^{\mathrm{I}} \cup \tilde{\mathcal{F}}_h^{\Gamma}$, where $\tilde{\mathcal{F}}_h^{\mathrm{I}} = \tilde{\mathcal{F}}_h \cap \mathcal{F}_h^{\mathrm{I}}$ and $\tilde{\mathcal{F}}_h^{\Gamma} = \tilde{\mathcal{F}}_h \cap \mathcal{F}_h^{\Gamma}$. Then

$$\int_{\tilde{\mathcal{F}}_h} \chi\,|\{\!\!\{\nabla_h v_h\}\!\!\}|^2\,\mathrm{d}S = \int_{\tilde{\mathcal{F}}_h^{\mathrm{I}}} \chi\,|\{\!\!\{\nabla_h v_h\}\!\!\}|^2\,\mathrm{d}S + \int_{\tilde{\mathcal{F}}_h^{\Gamma}} \chi\,|\nabla_h v_h|^2\,\mathrm{d}S$$

$$= \frac{1}{4}\int_{\tilde{\mathcal{F}}_h^{\mathrm{I}}} \chi\,\left|\nabla_h v_h^{(1)} + \nabla_h v_h^{(2)}\right|^2\,\mathrm{d}S + \int_{\tilde{\mathcal{F}}_h^{\Gamma}} \chi\,|\nabla_h v_h|^2\,\mathrm{d}S$$

$$\leq \frac{1}{2}\int_{\tilde{\mathcal{F}}_h^{\mathrm{I}}} \chi\,\left|\nabla_h v_h^{(1)}\right|^2 + \chi\,\left|\nabla_h v_h^{(2)}\right|^2\,\mathrm{d}S + \int_{\tilde{\mathcal{F}}_h^{\Gamma}} \chi\,|\nabla_h v_h|^2\,\mathrm{d}S \quad (1.48c)$$

$$\leq \sum_{K \in \mathcal{T}_h} \chi_K\,\|\nabla_h v_h\|_{0,\partial K}^2$$

$$\leq \sum_{K \in \mathcal{T}_h} C_{\mathrm{tinv}}^2 h_K^{-1}\chi_K\,\|\nabla_h v_h\|_{0,K}^2\,,$$

where $\chi_K := \max\left(\max\left\{\frac{1}{2}\chi_F\;;\;F \subset \partial K \cap \tilde{\mathcal{F}}_h^{\mathrm{I}}\right\}, \max\left\{\chi_F\;;\;F \subset \partial K \cap \tilde{\mathcal{F}}_h^{\Gamma}\right\}\right)$, which leads to

$$-2\,\mathrm{Re}\int_{\tilde{\mathcal{F}}_h} [\![v_h]\!] \cdot \overline{\{\!\!\{\nabla_h v_h\}\!\!\}}\,\mathrm{d}S \geq -\left\|\chi^{-1/2}[\![v_h]\!]\right\|_{0,\tilde{\mathcal{F}}_h}^2 - \sum_{K \in \mathcal{T}_h} C_{\mathrm{tinv}}^2 h_K^{-1}\chi_K\,\|\nabla_h v_h\|_{0,K}^2\,. \quad (1.48d)$$

We will apply (1.48d) to $\tilde{\mathcal{F}}_h = \mathcal{F}_h^{\mathrm{I}} \cup \mathcal{F}_h^{\mathrm{D}}$ with $\chi = \mathsf{h}\mu$ and (1.48b) to $\tilde{\mathcal{F}}_h = \mathcal{F}_h^{\mathrm{R}}$ with $\chi = 1/\nu\omega$ for arbitrary $\mu, \nu > 0$ constant on each $F \in \mathcal{F}_h$. The notation μ_K is analogous to χ_K above. Using $\mathsf{h} \leq h_K$ and (1.48a), we can estimate

$$|b_h(v_h, v_h)| \geq \frac{1}{\sqrt{2}}\left[|\mathrm{Re}\,b_h(v_h, v_h)| + |\mathrm{Im}\,b_h(v_h, v_h)|\right]$$

$$\geq \frac{1}{\sqrt{2}}\Bigg[\sum_{K \in \mathcal{T}_h} \left(1 - C_{\mathrm{tinv}}^2\mu_K\right)\|\nabla_h v_h\|_{0,K}^2 + \omega^2\|v_h\|_{0,\Omega}^2$$

$$+ \int_{\mathcal{F}_h^{\mathrm{I}}} \left(1 - \frac{1}{\mathsf{a}\mu}\right)\frac{\mathsf{a}}{\mathsf{h}}\,|[\![v_h]\!]|^2\,\mathrm{d}S + \int_{\mathcal{F}_h^{\mathrm{D}}} \left(1 - \frac{1}{\mathsf{a}\mu}\right)\frac{\mathsf{a}}{\mathsf{h}}\,|v_h|^2\,\mathrm{d}S$$

$$+ \omega\int_{\mathcal{F}_h^{\mathrm{R}}} \left(1 - \nu\frac{\delta}{1 - \delta}\right)(1 - \delta)\,|v_h|^2\,\mathrm{d}S \quad (1.48e)$$

$$+ \omega^{-1}\int_{\mathcal{F}_h^{\mathrm{R}}} \left(1 - \frac{1}{\nu}\right)\delta\,|\nabla_h v_h \cdot \boldsymbol{n}|^2\,\mathrm{d}S$$

$$+ \mathrm{i}\omega^{-1}\left\|\beta^{1/2}[\![\nabla_h v_h]\!]\right\|_{0,\mathcal{F}_h^{\mathrm{I}}}^2 + \mathrm{i}\omega^{-1}\left\|\beta^{1/2}\nabla_h v_h \cdot \boldsymbol{n}\right\|_{0,\mathcal{F}_h^{\mathrm{N}}}^2\Bigg]\,.$$
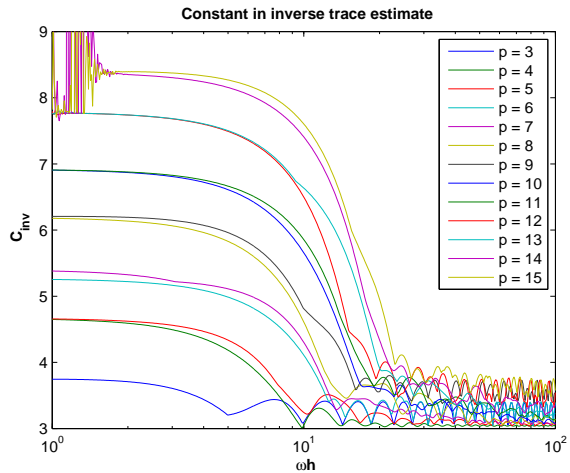
Figure 1.1: C_{tinv} on equilateral triangle K with $V_h(K) = PW_\omega^{p,0}(K)$.

Thus $|b_h(v_h, v_h)|$ can be bounded from below by a constant C_{coer} times $\|v_h\|_{\text{DG}}^2$ if all of the factors in the integrals in (1.48e) are positive, with C_{coer} equal to the smallest of these factors. This is the case if

$$C_{\text{tinv}}^2 < \frac{1}{\mu_K} \leq \frac{2}{\mu_F} < 2\mathsf{a} \qquad \text{for } F \in \mathcal{F}_h^{\text{I}} , \tag{1.48f}$$

$$C_{\text{tinv}}^2 < \frac{1}{\mu_K} \leq \frac{1}{\mu_F} < \mathsf{a} \qquad \text{for } F \in \mathcal{F}_h^{\text{D}} , \tag{1.48g}$$

$$\frac{\delta}{1-\delta} < \frac{1}{\nu_F} < 1 \qquad \text{for } F \in \mathcal{F}_h^{\text{R}} , \tag{1.48h}$$

where $K \in \mathcal{T}_h$ in the upper two equations is understood to contain F as a face. Equation (1.48h) can be fulfilled whenever $\delta < 1/2$. Equations (1.48f) and (1.48g) can be satisfied if $\mathsf{C}_{\text{tinv}}^2 < 2\mathsf{a}$ on $\mathcal{F}_h^{\text{I}}$ and $\mathsf{C}_{\text{tinv}}^2 < \mathsf{a}$ on $\mathcal{F}_h^{\text{D}}$, since one can then choose μ_F such that $\mathsf{C}_{\text{tinv}}^2 < 2/\mu_F < 2\mathsf{a}$ for $F \in \mathcal{F}_h^{\text{I}}$ and $\mathsf{C}_{\text{tinv}}^2 < 1/\mu_F < \mathsf{a}$ for $F \in \mathcal{F}_h^{\text{D}}$. It follows from the definition of C_{tinv} that $C_{\text{tinv}}(K)^2 < 2/\mu_F$ for $F \in \mathcal{F}_h^{\text{I}}$ and $C_{\text{tinv}}(K)^2 < 1/\mu_F$ for $F \in \mathcal{F}_h^{\text{D}}$, where $F \subset \partial K$. Therefore, by the definition of μ_K, $C_{\text{tinv}}^2 < 1/\mu_K$.

$\qquad\qquad\qquad\qquad\qquad\qquad\qquad\qquad\qquad\qquad\qquad\qquad\qquad\qquad\qquad\square$

The above proposition suggests that the choice of flux parameters should depend on C_{tinv}. Figure 1.1 shows numerically computed values of $C_{\text{tinv}}(K)$ as a function of ωh_K on an equilateral triangle K, using $V_h(K) = PW_\omega^{p,0}(K)$ for various p. These values are very similar to those obtained by Hiptmair and Perugia in [12, Section 4] for squares and various right triangles using odd p.

Apparently, for small ωh_K, C_{tinv} increases linearly in $p^{(\text{iv})}$. Interestingly, the value for an even value of p is almost identical to that for the next larger odd p. Also, as shown in [12] for odd p, C_{tinv} seems to stay bounded as ωh_K goes to zero.

For large values of ωh_K, C_{tinv} decreases significantly and seems to be bounded almost independently of p.

The implications for the flux parameters are that, assuming

$$\alpha = \frac{\mathsf{a}}{\omega \mathsf{h}} \sim \frac{\mathsf{C}_{\text{tinv}}^2}{\omega \mathsf{h}} , \tag{1.49}$$

then

$$\alpha \sim \begin{cases} \mathsf{p}^2/\omega\mathsf{h}, & \text{for } \omega\mathsf{h} \text{ small} \\ 1/\omega\mathsf{h}, & \text{for } \omega\mathsf{h} \text{ large} \end{cases} , \tag{1.50}$$

where $\mathsf{p}(F) = \max\{p(K)\,;\,F \subset \partial K\}$. In particular, these considerations suggest that for small $\omega\mathsf{h}$, α should be chosen significantly larger than the constant value (1.39) corresponding to the ultra-weak variational method, and for large $\omega\mathsf{h}$, α should be smaller than that value.

(iv) The strong oscillations for $p \in \{14, 15\}$ in Figure 1.1 are due to numerical errors. The computations were done using plane wave basis functions, which become unstable for small ωh_K or large p.

Chapter 2

Aspects of implementation in two dimensions

Plane wave basis functions present some difficulties in the implementation of DG methods. In this chapter, we discuss an efficient method for constructing many relevant matrices and ways to handle curved edges in the mesh.

2.1 Assembly

Discontinuous Galerkin methods can be derived locally on elements of the mesh; therefore, a straightforward assembly procedure for the mass matrix or stiffness matrix[i] is to loop over all elements of the mesh and compute the local contributions. This is not, however, the optimal approach for PWDG methods.

The variational form (1.27) for primal PWDG methods can be computed through integrals over the faces of the mesh alone. It therefore makes sense to construct the stiffness matrix by assembling only local contributions of the faces of the mesh, and not the elements. This is described in detail in Section 2.1.1 for the two-dimensional case.

Even though the mass matrix is block-diagonal with blocks corresponding to the elements of the mesh, it turns out that it too can be assembled more efficiently over the faces of the mesh, see Section 2.1.2.

2.1.1 Stiffness matrix

The local contributions to the stiffness matrix are integrals corresponding to the left-hand side of (1.27) over a single edge[ii] $F \in \mathcal{F}_h$, where the test function v_h is a plane wave $e^{i\omega \boldsymbol{d_2} \cdot \boldsymbol{x}}$ restricted to one of the neighboring elements and the approximate solution is of the same form, $u_h = e^{i\omega \boldsymbol{d_1} \cdot \boldsymbol{x}}$, also restricted to one of the neighboring elements.

Assume that the fluxes preserve the plane wave character of the approximate solution, that is, that $\widehat{u}_h$ and the components of $\widehat{\boldsymbol{\sigma}}_h$ restricted to F are in the span of the plane wave basis functions of the two neighboring elements. This

---

[i] The stiffness matrix is the discretization of the full Helmholtz operator $-\Delta - \omega^2$, not just the Laplacian $-\Delta$.
[ii] in general: a single face

is the case for fluxes of the form (1.35). The assumption implies that, for $u_h = e^{i\omega \boldsymbol{d_1} \cdot \boldsymbol{x}}$, the fluxes are a scalar multiplied by the same plane wave[iii]. Therefore, the contribution of F to the stiffness matrix is a complex number times

$$\int_F e^{i\omega \boldsymbol{d_1} \cdot \boldsymbol{x}} \overline{e^{i\omega \boldsymbol{d_2} \cdot \boldsymbol{x}}} \, dS = \int_F e^{i\omega \boldsymbol{d} \cdot \boldsymbol{x}} \, dS \,, \tag{2.1}$$

with $\boldsymbol{d} = \boldsymbol{d_1} - \boldsymbol{d_2}$. The computation of the constant factor is straightforward; it can be obtained by inserting the plane wave basis functions into the left-hand side of (1.27) and factoring out (2.1).

Let the edge F be parameterized by $\boldsymbol{\gamma} : [0,1] \to F \subset \mathbb{R}^2$, $t \mapsto \boldsymbol{a} + t(\boldsymbol{b} - \boldsymbol{a})$. Then

$$\int_F e^{i\omega \boldsymbol{d} \cdot \boldsymbol{x}} \, dS = e^{i\omega \boldsymbol{d} \cdot \boldsymbol{a}} \, |\boldsymbol{b} - \boldsymbol{a}| \int_0^1 e^{i\omega \boldsymbol{d} \cdot (\boldsymbol{b} - \boldsymbol{a})t} \, dt \,. \tag{2.2}$$

Using

$$\psi(z) := \int_0^1 e^{zt} \, dt = \begin{cases} \dfrac{e^z - 1}{z}, & z \neq 0 \\ 1, & z = 0 \end{cases} \,, \tag{2.3}$$

we can write

$$\int_F e^{i\omega \boldsymbol{d} \cdot \boldsymbol{x}} \, dS = e^{i\omega \boldsymbol{d} \cdot \boldsymbol{a}} \, |\boldsymbol{b} - \boldsymbol{a}| \, \psi(i\omega \boldsymbol{d} \cdot (\boldsymbol{b} - \boldsymbol{a})) \,. \tag{2.4}$$

Thus the contribution of F to the stiffness matrix can be computed analytically.

However, care must be taken in the evaluation of ψ for small nonzero arguments since direct evaluation of the formula given in (2.3) is prone to cancellation. This can be done by computing the numerator with Matlab's `expm1` routine, which amounts to precomputing e^z and then evaluating

$$\psi(z) = \frac{e^z - 1}{\log e^z} \tag{2.5}$$

for problematic arguments z[iv].

Apparently, the L_2-inner product matrix (2.1) on the edge F is used to construct the stiffness matrix. Of course, this inner product matrix is hermitian and therefore only the upper (or lower) triangular part needs to be computed.

2.1.2 Inner product matrices

It is somewhat surprising that the entries of the mass matrix, which initially are volume integrals, can also be computed using only integrals over the edges of the mesh.

[iii] Take $e^{i\omega \boldsymbol{d_1} \cdot \boldsymbol{x}}$ as the only basis function.
[iv] A comment in `expm1.m` cites unpublished course notes of W. Kahan as the reference for this algorithm.

On an element $K \in \mathcal{T}_h$, using $\boldsymbol{d} = \boldsymbol{d}_1 - \boldsymbol{d}_2 \neq \boldsymbol{0}$ and $\Delta \mathrm{e}^{\mathrm{i}\omega \boldsymbol{d} \cdot \boldsymbol{x}} = -\omega^2 \boldsymbol{d} \cdot \boldsymbol{d} \, \mathrm{e}^{\mathrm{i}\omega \boldsymbol{d} \cdot \boldsymbol{x}}$,

$$\int_K \mathrm{e}^{\mathrm{i}\omega \boldsymbol{d}_1 \cdot \boldsymbol{x}} \, \overline{\mathrm{e}^{\mathrm{i}\omega \boldsymbol{d}_2 \cdot \boldsymbol{x}}} \, \mathrm{d}\boldsymbol{x} = \int_K \mathrm{e}^{\mathrm{i}\omega \boldsymbol{d} \cdot \boldsymbol{x}} \, \mathrm{d}\boldsymbol{x} \tag{2.6a}$$

$$= \frac{-1}{\omega^2 \boldsymbol{d} \cdot \boldsymbol{d}} \int_K \Delta \mathrm{e}^{\mathrm{i}\omega \boldsymbol{d} \cdot \boldsymbol{x}} \, \mathrm{d}\boldsymbol{x} \tag{2.6b}$$

$$= \frac{-1}{\omega^2 \boldsymbol{d} \cdot \boldsymbol{d}} \int_{\partial K} \nabla \mathrm{e}^{\mathrm{i}\omega \boldsymbol{d} \cdot \boldsymbol{x}} \cdot \boldsymbol{n} \, \mathrm{d}S \tag{2.6c}$$

$$= \sum_{F \in \partial K \cap \mathcal{F}_h} \frac{-\mathrm{i}\omega \boldsymbol{d} \cdot \boldsymbol{n}}{\omega^2 \boldsymbol{d} \cdot \boldsymbol{d}} \int_F \mathrm{e}^{\mathrm{i}\omega \boldsymbol{d} \cdot \boldsymbol{x}} \, \mathrm{d}S \, , \tag{2.6d}$$

where $\boldsymbol{n} = \binom{n_1}{n_2}$ is the exterior normal to K. The integrals in the last term can be evaluated using (2.4).

Of course, for $\boldsymbol{d}_1 = \boldsymbol{d}_2$, the entry of the mass matrix is simply the area of K. This can also be computed via the skeleton of the mesh using, for example, $1 = \frac{1}{2}\Delta x_1^2$,

$$\int_K \mathrm{e}^{\mathrm{i}\omega \boldsymbol{d}_1 \cdot \boldsymbol{x}} \, \overline{\mathrm{e}^{\mathrm{i}\omega \boldsymbol{d}_1 \cdot \boldsymbol{x}}} \, \mathrm{d}\boldsymbol{x} = \int_K 1 \, \mathrm{d}\boldsymbol{x} \tag{2.7a}$$

$$= \frac{1}{2} \int_K \Delta x_1^2 \, \mathrm{d}\boldsymbol{x} \tag{2.7b}$$

$$= \frac{1}{2} \int_{\partial K} \nabla x_1^2 \cdot \boldsymbol{n} \, \mathrm{d}S \tag{2.7c}$$

$$= \sum_{F \in \partial K \cap \mathcal{F}_h} \int_F x_1 n_1 \, \mathrm{d}S \, . \tag{2.7d}$$

The last term can be evaluated easily using the same parameterization of F as above.

Note that if the basis functions on two neighboring elements coincide, then the same integral over the shared edge contributes to both local mass matrices (up to the sign of the exterior normal vector). Since the assembly procedure runs over edges, this term can be computed once and immediately passed on to both elements.

Also, as for the stiffness matrix, the integrals in (2.6d) are entries of the L_2-inner product matrix on the edge F and therefore only half of these need to be computed. Of course, if both the mass and stiffness matrices are required, these terms may be precomputed.

The entries of other inner product matrices can be reduced to those of the mass matrix. For example, the entries of the H_0^1-inner product matrix are

$$\int_K \nabla \mathrm{e}^{\mathrm{i}\omega \boldsymbol{d}_1 \cdot \boldsymbol{x}} \cdot \overline{\nabla \mathrm{e}^{\mathrm{i}\omega \boldsymbol{d}_2 \cdot \boldsymbol{x}}} \, \mathrm{d}\boldsymbol{x} = \omega^2 \boldsymbol{d}_1 \cdot \boldsymbol{d}_2 \int_K \mathrm{e}^{\mathrm{i}\omega \boldsymbol{d}_1 \cdot \boldsymbol{x}} \, \overline{\mathrm{e}^{\mathrm{i}\omega \boldsymbol{d}_2 \cdot \boldsymbol{x}}} \, \mathrm{d}\boldsymbol{x} \, . \tag{2.8}$$

2.2 Curved edges

2.2.1 Boundary integrals

Of course, the approaches discussed in Sections 2.1.1 and 2.1.2 for the construction of the stiffness matrix and inner product matrices for plane wave basis functions also work on meshes with curved edges.

Consider an edge $F \in \mathcal{F}_h$ parameterized by an arbitrary, sufficiently smooth function $\boldsymbol{\gamma} : [0,1] \to F \subset \mathbb{R}^2$. Equation (2.2) generalizes to

$$\int_F \mathrm{e}^{\mathrm{i}\omega \boldsymbol{d} \cdot \boldsymbol{x}} \, \mathrm{d}S = \int_0^1 \mathrm{e}^{\mathrm{i}\omega \boldsymbol{d} \cdot \boldsymbol{\gamma}(t)} \, |\dot{\boldsymbol{\gamma}}(t)| \, \mathrm{d}t \, , \tag{2.9}$$

which can be evaluated using a quadrature rule.

The arguments in (2.6) and (2.7) still hold, with the exception that the exterior normal vector $\boldsymbol{n}$ is no longer constant and therefore $\boldsymbol{d} \cdot \boldsymbol{n}$ must remain inside the integral in (2.6d). Again, numerical quadrature can be used to evaluate the resulting integrals.

2.2.2 Volume integrals

No volume integrals are required for the construction of relevant matrices; however, they are unavoidable in the computation of the load vector for inhomogeneous problems as well as approximation errors when the exact solution is known.

Two strategies can be used to compute integrals over elements with curved edges. A quadrature rule could be constructed directly on the element, or using a smooth enough parametrization of the element. Alternatively, the element could be approximated by triangles (or other polygons) for which well-known quadrature rules exist. Of course, this approximation can be refined towards the curved edges[v].

---

[v]This strategy is applied in the code used for the experiments in this paper.

Chapter 3

Convergence Experiments

The numerical experiments presented in this chapter demonstrate the convergence of the h-version of plane wave discontinuous Galerkin methods in two dimensions.

3.1 Preliminaries

3.1.1 Model problems

The numerical experiments presented in Sections 3.2 and 5.1 are based on the boundary value problem (1.1) in the following settings.

Model Problem 1 is a homogeneous boundary value problem on the unit square $\Omega =]0,1[^2$ with Robin boundary conditions, ie. $\partial\Omega = \Gamma^{\mathrm{R}}$. The boundary term g^{R} is chosen such that the exact solution is a plane wave propagating in the first coordinate direction,

$$u(\boldsymbol{x}) = \mathrm{e}^{\mathrm{i}\omega\boldsymbol{d}\cdot\boldsymbol{x}} = \mathrm{e}^{\mathrm{i}\omega x_1} , \qquad \boldsymbol{d} = \begin{pmatrix} 1 \\ 0 \end{pmatrix} . \tag{3.1}$$

We will consider this problem for various wavenumbers ω. The corresponding wavelengths are $\lambda = \frac{2\pi}{\omega}$.

Model Problem 2 is, like Model Problem 1, a homogeneous boundary value problem on $\Omega =]0,1[^2$ with Robin boundary conditions. The boundary term g^{R} is chosen such that the exact solution is a cylindrical wave emanating from a point outside the domain,

$$u(\boldsymbol{x}) = H_0^{(1)}(\omega|\boldsymbol{x} - \boldsymbol{x}_0|) , \qquad \boldsymbol{x}_0 = \begin{pmatrix} -1/4 \\ 0 \end{pmatrix} . \tag{3.2}$$

Model Problem 3 is a more realistic homogeneous boundary value problem. It models the reflection of the plane wave (3.1) on the sound-soft unit circle. The exact reflected wave, given in polar coordinates, is

$$u(r,\varphi) = -\frac{J_0(\omega)}{H_0^{(2)}(\omega)} H_0^{(2)}(\omega r) - 2\sum_{n=1}^{\infty} \mathrm{i}^n \frac{J_n(\omega)}{H_n^{(2)}(\omega)} H_n^{(2)}(\omega r) \cos(n\varphi) . \tag{3.3}$$
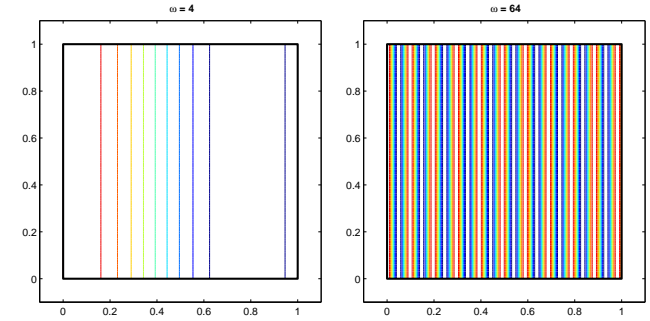
Figure 3.1: The exact solution of Model Problem 1 for $\omega = 4$ and $\omega = 64$.
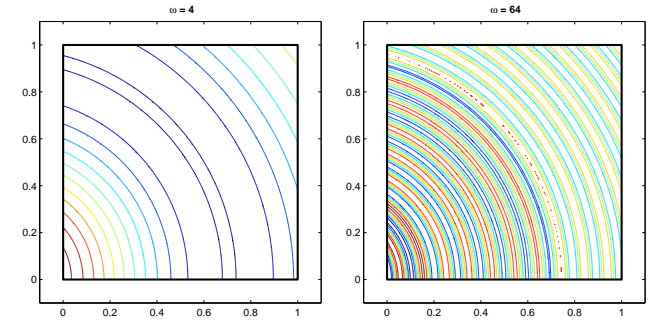
Figure 3.2: The exact solution of Model Problem 2 for $\omega = 4$ and $\omega = 64$.
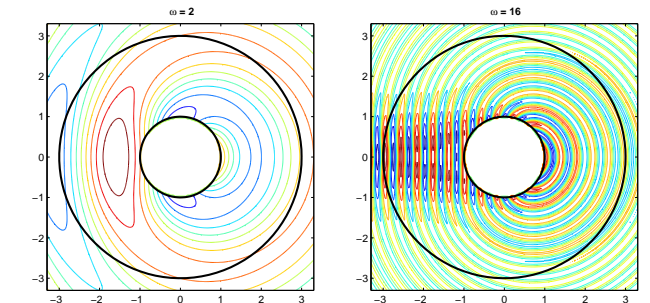
Figure 3.3: The exact solution of Model Problem 3 for $\omega = 2$ and $\omega = 16$ with the superimposed computational domain.

We solve for this on the annulus $\Omega = \left\{ \boldsymbol{x} \in \mathbb{R}^2 \; ; \; 1 < \boldsymbol{x} < 3 \right\}$ using Dirichlet boundary conditions on the inner boundary and Robin boundary conditions that take into account the exact solution on the exterior boundary.

Model Problem 4 is an inhomogeneous version of Model Problem 1. The exact solution is a plane wave with wavenumber $\frac{\omega}{2}$,

$$u(\boldsymbol{x}) = \mathrm{e}^{\mathrm{i}\frac{\omega}{2}\boldsymbol{d}\cdot\boldsymbol{x}} = \mathrm{e}^{\mathrm{i}\frac{\omega}{2}x_1} , \qquad \boldsymbol{d} = \begin{pmatrix} 1 \\ 0 \end{pmatrix} . \tag{3.4}$$

3.1.2   Discretization

We consider four variants of the plane wave discontinuous Galerkin method. These have fluxes of the form form (1.35) and are defined by the parameters listed in Table 3.1. In the following, PWDG will refer to any of these methods and PWDG_i will refer to PWDG_0, PWDG_1 and PWDG_2.

Table 3.1: Flux parameters used in numerical experiments

Name	$\alpha\vert_{\mathcal{F}_h^{\mathrm{I}}}$	$\alpha\vert_{\mathcal{F}_h^{\mathrm{D}}}$	β	$\boldsymbol{\gamma}$	δ
UWVF	$\frac{1}{2}$		$\frac{1}{2}$	$\boldsymbol{0}$	$\frac{1}{2}$
PWDG_0	$\frac{2}{\omega\mathbf{h}}$		0	$\boldsymbol{0}$	0
PWDG_1	$\frac{\mathtt{c}_{\mathrm{tinv}}^2}{2\omega\mathbf{h}}$	$\frac{\mathtt{c}_{\mathrm{tinv}}^2}{\omega\mathbf{h}}$	0	$\boldsymbol{0}$	0
PWDG_2	$\frac{\mathtt{c}_{\mathrm{tinv}}^2}{2\omega\mathbf{h}}$	$\frac{\mathtt{c}_{\mathrm{tinv}}^2}{\omega\mathbf{h}}$	$\frac{\omega\mathbf{h}}{10}$	$\boldsymbol{0}$	$\min(\frac{\omega\mathbf{h}}{10}, \frac{1}{2})$

Note that UWVF is the ultra-weak variational method described in Section 1.3.3. The PWDG_i methods use flux parameters of the form (1.36). In particular, PWDG_1 and PWDG_2 almost satisfy the assumptions of Proposition 1.7 in the sense that the parameters lie in the closure of the admissible set.

Unless stated otherwise, the experiments are performed on fairly uniform unstructured triangular meshes. Some of these are plotted in Figure 3.4 for the unit square and Figure 3.5 for the annulus. The curved edges in the meshes of the annulus are parameterized exactly; matrix entries are computed by high-order quadrature on these curved edges and using analytical formulas on straight edges[i]. The mesh width h is the mean diameter of all of the elements of the mesh.

We restrict ourselves to local plane wave spaces with equidistantly spaced basis functions. For Model Problems 2 and 3, the local spaces are of the form $PW_\omega^{p,0}(K)$ for some p; for Model Problems 1 and 4, we use $PW_\omega^{p,\frac{\pi}{p}}(K)$ to prevent the exact solution from being in the discrete space. In both cases, we will simply refer to the parameter p.

---
[i]See Chapter 2 for details.
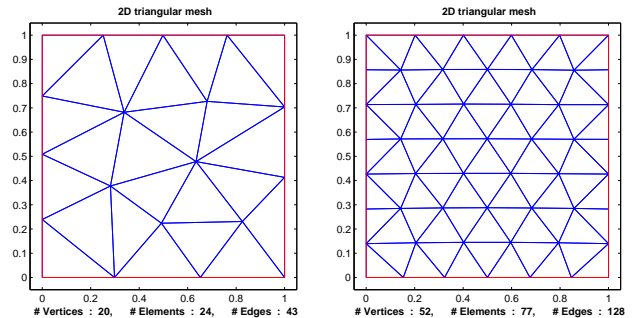
Figure 3.4: The fourth and sixth coursest of twenty-one meshes used in convergence experiments on the unit square.
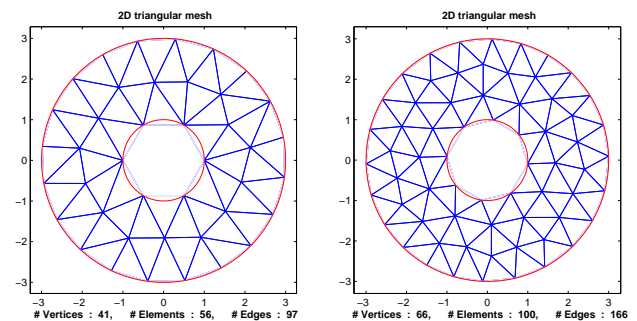
Figure 3.5: The two coarsest of ten meshes used in convergence experiments on the annulus.

3.1.3 Experiment setup

Errors are monitored in the L_2-norm $\|\cdot\|_{0,\Omega}$ and in the broken weighted Sobolev norm

$$\|v\|^2_\omega := \|\nabla_h v\|^2_{0,\Omega} + \omega^2 \|v\|^2_{0,\Omega} \ , \tag{3.5}$$

which we will in the following call the *energy norm*. Errors are computed by high-order quadrature, using analytical formulas for the exact solutions and their gradients.

Estimates of the asymptotic convergence rate of the best approximation as $\omega h \to 0$ are given; these are computed by the following heuristic. First a 'convergence domain' is determined where the error depends monotonously on ωh; more precisely, this is the largest domain in which the slope of the convergence curve in bilogarithmic scale is at least $\frac{3}{4}$(ii). On this domain, the error is then approximated by a line in bilogarithmic scale using linear regression, where the equations corresponding to the individual data points are weighted by $(\omega h)^{-2}$ to capture the asymptotic behavior. The slope of this line is the approximate convergence rate.

All of the experiments were performed in Matlab 7.4.0 (R2007a), relying on the standard 'backslash' solver to directly solve the resulting linear systems. The implementation of the plane wave DG method is part of the *LehrFEM* finite element toolkit. It directly uses plane waves as basis functions.

The use of the plane wave basis causes some instabilities for small ωh. The inversion of the mass matrix is particularly sensitive; accordingly, the error of the best approximation in the L_2-norm seems to diverge for small ωh in some of the figures in the following sections. This is due only to numerical issues and does not reflect the behavior of the actual projection error.

3.2 Convergence results

In this section, we consider experimental results concerning the h-asymptotic behavior of plane wave DG methods. Experiments that study the preasymptotic ω-dependence of the convergence behavior are presented in Section 5.1.

Figures 3.6 and 3.7 show convergence curves for the inhomogeneous Model Problem 4 for $\omega = 4$ and $\omega = 64$, respectively, with $p = 5$ local basis functions. All of the PWDG methods display linear convergence in the energy norm. In the L_2-norm, the ultra-weak method still has convergence rate one, but the PWDG$_i$ methods display quadratic convergence.

Figure 3.8 shows that the convergence rates of PWDG$_2$ are independent of p for the inhomogeneous problem. It seems to be inefficient to increase p beyond a certain value; in this example, $p = 5$ is optimal.

The situation is drastically different in the homogeneous case. Figures 3.9, 3.10, 3.13 and 3.14 show convergence curves for Model Problems 1 and 3 with $p = 5$. Similar plots for Model Problem 2 can be found in [12, Section 7]. All of the PWDG methods display quadratic convergence in the energy norm and cubic convergence in the L_2-norm.

Figure 3.11 shows that there is a clear gain in efficiency in using large p for homogeneous problems. Figure 3.12 indicates that convergence rates for odd

---
(ii)Occasionally, this heuristic led to inaccurate results and the relevant domain was selected manually.

$p = 2m - 1$ are the same as for even $p = 2m$. However, there is still a slight gain in accuracy in using even p. These results are confirmed by Figures 3.15 and 3.16 for Model Problem 3.

Some numerically determined asymptotic convergence rates of the best approximation in the energy norm are listed in Table 3.2. Values with highly questionable accuracy due to stability issues are preceded by '†'. The last two columns show whole-number values close to the numerically determined convergence rates. In the homogeneous case, these are determined by the formula $\lceil \frac{p}{2} \rceil - 1$, where $\lceil x \rceil$ denotes the smallest whole number greater than or equal to x. For inhomogeneous problems, the convergence rate is always near one. Hiptmair and Perugia present corresponding h-convergence theory in [12, Section 5].

Convergence rates in the L_2-norm seem to be one higher than in the energy norm for PWDG$_i$ methods. This often, but not always, also holds for UWVF.

Table 3.2: Numerically determined convergence rates in energy norm

p	Prob. 1		Prob. 3		Prob. 4		hom.	inhm.
	$\omega = 4$	$\omega = 64$	$\omega = 2$	$\omega = 16$	$\omega = 4$	$\omega = 64$	$\lceil \frac{p}{2} \rceil - 1$	1
3	0.98	0.94	1.03	0.88	0.98	0.98	1	1
4	0.98	1.01	1.09	1.08	0.97	0.98	1	1
5	1.96	1.93	2.02	1.74	0.97	0.97	2	1
6	1.95	1.89	2.00	1.95	0.96	1.01	2	1
7	2.81	2.78	2.79	2.73	0.96	0.99	3	1
8	2.91	2.86	2.75	2.89	–	–	3	1
9	†3.14	3.69	†2.72	3.65	0.95	0.97	4	1
10	†3.14	3.78	†3.17	3.60	–	–	4	1
11	†4.29	4.67	†4.17	†3.61	0.95	0.97	5	1
13	†4.12	5.53	–	†4.78	0.94	0.96	6	1
15	–	6.37	–	†4.90	0.94	0.95	7	1

All of the convergence experiments presented so far study the asymptotic convergence behavior of PWDG. For large wave numbers, however, this may only apply to extremely fine meshes. Highly relevant preasymptotic effects are studied in Chapter 5. These are related to dispersion and dissipation, which we turn to in the following Chapter 4.
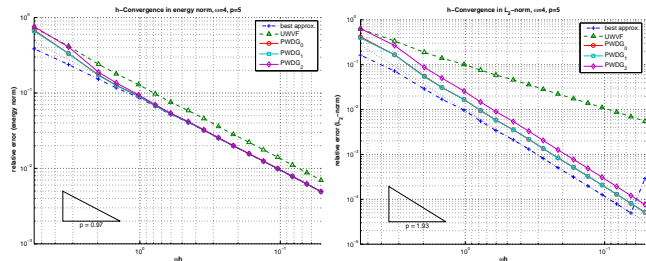
Figure 3.6: Model Problem 4: h-convergence of PWDG methods for $\omega = 4$ and $p = 5$. The relative errors in the energy norm and the L_2-norm are plotted against ωh.
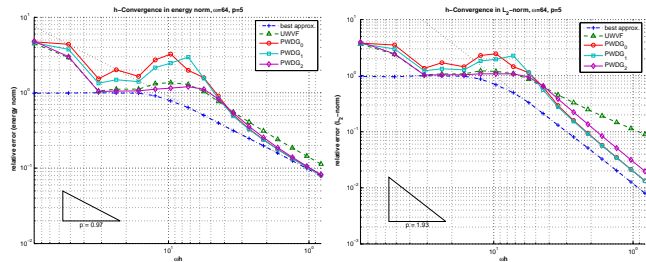

Figure 3.7: Model Problem 4: h-convergence of PWDG methods for $\omega = 64$ and $p = 5$. The relative errors in the energy norm and the L_2-norm are plotted against ωh.
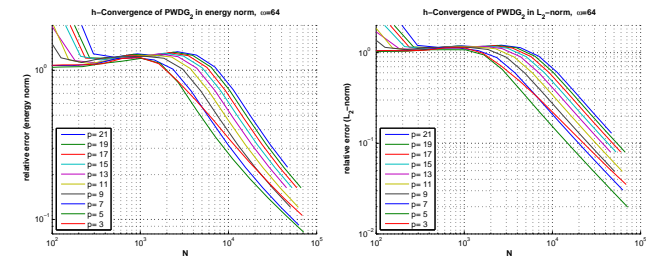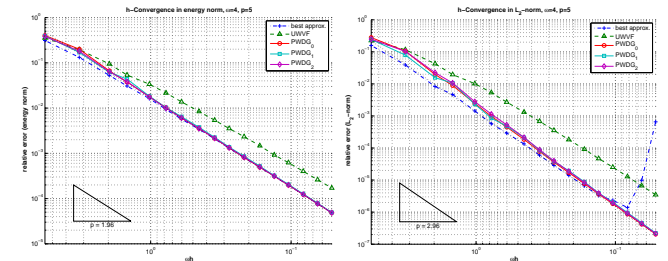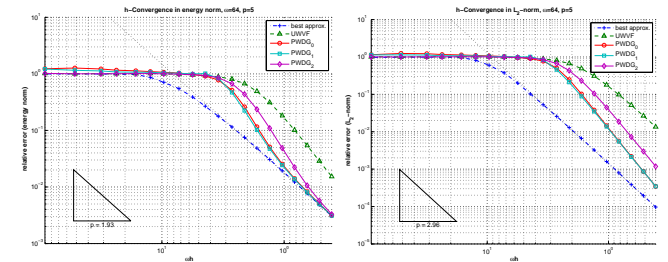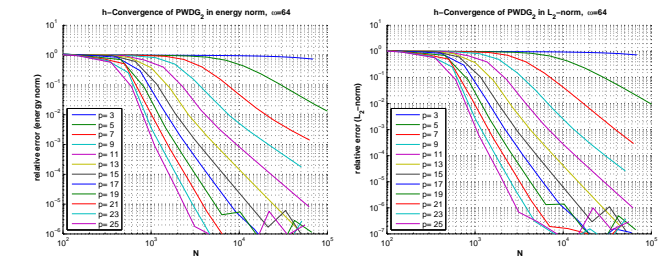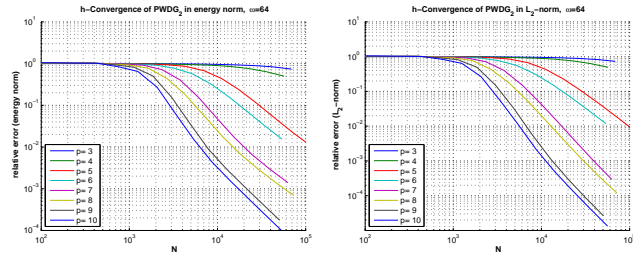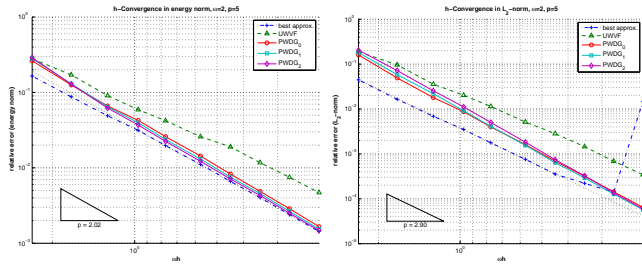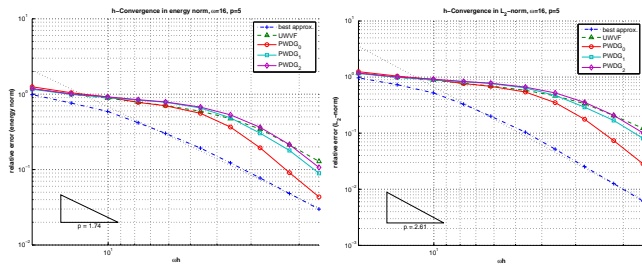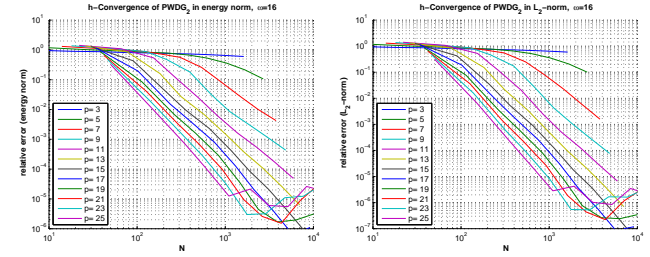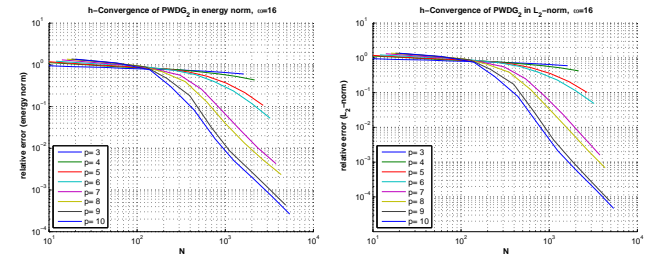

Figure 3.8: Model Problem 4: h-convergence of PWDG$_2$ for $\omega = 64$. The relative errors in the energy norm and the L_2-norm are plotted against the total number of degrees of freedom N for various p.

Figure 3.9: Model Problem 1: h-convergence of PWDG methods for $\omega = 4$ and $p = 5$. The relative errors in the energy norm and the L_2-norm are plotted against ωh.

Figure 3.10: Model Problem 1: h-convergence of PWDG methods for $\omega = 64$ and $p = 5$. The relative errors in the energy norm and the L_2-norm are plotted against ωh.

Figure 3.11: Model Problem 1: h-convergence of PWDG$_2$ for $\omega = 64$. The relative errors in the energy norm and the L_2-norm are plotted against the total number of degrees of freedom N for various p.

Figure 3.12: Model Problem 1: h-convergence of $PWDG_2$ for $\omega = 64$. The relative errors in the energy norm and the L_2-norm are plotted against the total number of degrees of freedom N for various even and odd p.

Figure 3.13: Model Problem 3: h-convergence of PWDG methods for $\omega = 2$ and $p = 5$. The relative errors in the energy norm and the L_2-norm are plotted against ωh.

Figure 3.14: Model Problem 3: h-convergence of PWDG methods for $\omega = 16$ and $p = 5$. The relative errors in the energy norm and the L_2-norm are plotted against ωh.

Figure 3.15: Model Problem 3: h-convergence of $PWDG_2$ for $\omega = 16$. The relative errors in the energy norm and the L_2-norm are plotted against the total number of degrees of freedom N for various p.

Figure 3.16: Model Problem 3: h-convergence of $PWDG_2$ for $\omega = 16$. The relative errors in the energy norm and the L_2-norm are plotted against the total number of degrees of freedom N for various even and odd p.

Chapter 4

Dispersion and dissipation

In this chapter, we experimentally determine the dispersive and dissipative properties of PWDG methods in two dimensions. The required translation invariant discretization on $\mathbb{R}^2$, as well as suitable definitions of dispersion and dissipation, are developed in a more general setting.

4.1 General framework

4.1.1 Translation invariant discretization on $\mathbb{R}^d$

Consider the homogeneous Helmholtz equation

$$- \Delta u - \omega^2 u = 0 \tag{4.1}$$

on the domain $\Omega = \mathbb{R}^d$.

Let $V_{h,\omega} \subset L_{2,\mathrm{loc}}(\mathbb{R}^d)$ be a possibly ω-dependent approximation space, $V_{h,\omega}^c$ denote the subspace of compactly supported functions in $V_{h,\omega}$, and let a_h be a sesquilinear form on $C^\infty(\mathbb{R}^d) + V_{h,\omega}$ for which the discretization of (4.1) reads: find $u_h \in V_{h,\omega}$ such that for all $v_h \in V_{h,\omega}^c$

$$a_{h,\omega}(u_h, v_h) := a_h(u_h, v_h) - \omega^2 (u_h, v_h)_{\mathbb{R}^d} = 0 , \tag{4.2}$$

cf. (1.43). We would like $V_{h,\omega}$ to have a translation invariance property such that (4.2) has almost periodic solutions in a sense that will be clarified below. To this end, for $\boldsymbol{\xi} \in \mathbb{R}^d$, we will define the translation $\tau_{\boldsymbol{\xi}} : C^\infty(\mathbb{R}^d) + V_{h,\omega} \to L_{2,\mathrm{loc}}(\mathbb{R}^d)$ by

$$(\tau_{\boldsymbol{\xi}} v)(\boldsymbol{x}) := v(\boldsymbol{x} - \boldsymbol{\xi}) . \tag{4.3}$$

Furthermore, we will call a sequence $(\boldsymbol{\xi_n})_{\boldsymbol{n}\in\mathbb{Z}^d}$ in $\mathbb{R}^d$ a *lattice* of $\mathbb{R}^d$ if there is a bijective linear map $G : \mathbb{R}^d \to \mathbb{R}^d$ such that $\boldsymbol{\xi_n} = G\boldsymbol{n}$ for all $\boldsymbol{n} \in \mathbb{Z}^d \subset \mathbb{R}^d$. We will assume in the following that a_h is translation invariant with respect to the lattice $(\boldsymbol{\xi_n})_{\boldsymbol{n}\in\mathbb{Z}^d}$ in the sense that

$$a_h(u_h, \tau_{\boldsymbol{n}} v_h) = a_h(\tau_{-\boldsymbol{n}} u_h, v_h) , \tag{4.4}$$

where $\tau_{\boldsymbol{n}} := \tau_{\boldsymbol{\xi_n}}$. Note that the same property immediately follows for $a_{h,\omega}$. We will now introduce a corresponding property for the approximation space $V_{h,\omega}$.

Definition 4.1. The space $V_{h,\omega}$ is *translation invariant* with respect to the lattice $(\boldsymbol{\xi_n})_{\boldsymbol{n}\in\mathbb{Z}^d}$ if for all $\boldsymbol{n} \in \mathbb{Z}^d$

$$\tau_{\boldsymbol{n}}(V_{h,\omega}) \subset V_{h,\omega} . \tag{4.5}$$

Remark 4.2. It follows immediately that $\tau_{\boldsymbol{n}}(V_{h,\omega}) = V_{h,\omega}$ for all $\boldsymbol{n} \in \mathbb{Z}^d$ since $\tau_{-\boldsymbol{n}} \circ \tau_{\boldsymbol{n}} = \mathrm{id}$.

We will consider translation invariant spaces $V_{h,\omega}$ of a form particularly suited to dispersion analysis of finite element methods. In the following, let $V_{h,\omega}$ be the translation invariant space generated by $\widehat{V}_{h,\omega}$ over the lattice $(\boldsymbol{\xi_n})_{\boldsymbol{n}\in\mathbb{Z}^d}$, as defined next.

Definition 4.3. Let $\widehat{V}_{h,\omega} \subset L_2(K) \subset L_{2,\mathrm{loc}}(\mathbb{R}^d)$ for a compact set $K \subset \mathbb{R}^d$, where the functions are extended to $\mathbb{R}^d$ by zero, and let $(\boldsymbol{\xi_n})_{\boldsymbol{n}\in\mathbb{Z}^d}$ be a lattice of $\mathbb{R}^d$. Assume that the spaces $(\tau_{\boldsymbol{n}}(\widehat{V}_{h,\omega}))_{\boldsymbol{n}\in\mathbb{Z}^d}$ have pairwise trivial intersection. Then for any complex sequence $(\alpha_{\boldsymbol{n}})_{\boldsymbol{n}\in\mathbb{Z}^d}$ and any sequence $(v_{h,\boldsymbol{n}})_{\boldsymbol{n}\in\mathbb{Z}^d}$ in $\widehat{V}_{h,\omega}$,

$$v_h := \sum_{\boldsymbol{n}\in\mathbb{Z}^d} \alpha_{\boldsymbol{n}} \tau_{\boldsymbol{n}}(v_{h,\boldsymbol{n}}) \tag{4.6}$$

is well defined in $L_{2,\mathrm{loc}}(\mathbb{R}^d)$ since the sum is locally finite. Therefore, the space

$$V_{h,\omega} := \sum_{\boldsymbol{n}\in\mathbb{Z}^d} \tau_{\boldsymbol{n}}\!\left(\widehat{V}_{h,\omega}\right) \tag{4.7}$$

consisting of all such (infinite) sums is a well defined subspace of $L_{2,\mathrm{loc}}(\mathbb{R}^d)$. We will call $V_{h,\omega}$ the *translation invariant space generated by* $\widehat{V}_{h,\omega}$ *over* $(\boldsymbol{\xi_n})_{\boldsymbol{n}\in\mathbb{Z}^d}$ and $\widehat{V}_{h,\omega}$ the *generator* of $V_{h,\omega}$.

Remark 4.4. It follows immediately from the definitions that the translation invariant space $V_{h,\omega}$ generated by $\widehat{V}_{h,\omega}$ is in fact translation invariant with respect to $(\boldsymbol{\xi_n})_{\boldsymbol{n}\in\mathbb{Z}^d}$. However, it is not the smallest translation invariant space containing $\widehat{V}_{h,\omega}$, since already $V_{h,\omega}^c$, which consists of all the finite sums of the form (4.6), is a translation invariant space. If $\widehat{V}_{h,\omega}$ is a closed subspace of $L_2(K)$, then $V_{h,\omega}$ is in fact the closure in $L_{2,\mathrm{loc}}(\mathbb{R}^d)$ of $V_{h,\omega}^c$.

The reason for taking infinite linear combinations is to have periodic or almost periodic functions in $V_{h,\omega}$. For any complex sequence $(\alpha_{\boldsymbol{n}})_{\boldsymbol{n}\in\mathbb{Z}^d}$, the space

$$\left(\sum_{\boldsymbol{n}\in\mathbb{Z}^d} \alpha_{\boldsymbol{n}} \tau_{\boldsymbol{n}}\right)\widehat{V}_{h,\omega} \tag{4.8}$$

is a subspace of $V_{h,\omega}$. It contains all elements of the form (4.6) with $(v_{h,\boldsymbol{n}})_{\boldsymbol{n}\in\mathbb{Z}^d}$ constant. Consider the case of $\alpha_{\boldsymbol{n}} = \mathrm{e}^{\mathrm{i}\omega_h \boldsymbol{d}\cdot\boldsymbol{\xi_n}}$ for some $\boldsymbol{d} \in S^{d-1} \subset \mathbb{R}^d$. Then the elements of (4.8) are almost periodic; they are Bloch waves.

Definition 4.5. A *Bloch wave* v_h in $V_{h,\omega}$ with propagation direction $\boldsymbol{d} \in S^{d-1} \subset \mathbb{R}^d$ is a function of the form

$$v_h = \sum_{\boldsymbol{n}\in\mathbb{Z}^d} \mathrm{e}^{\mathrm{i}\omega_h \boldsymbol{d}\cdot\boldsymbol{\xi_n}} \tau_{\boldsymbol{n}}(v_0) \tag{4.9}$$

for some $v_0 \in \widehat{V}_{h,\omega}$ and $\omega_h \in \mathbb{C}$ with $\mathrm{Re}\,\omega_h > 0$.

Bloch waves are characterized by the property[i]

$$(\tau_{-\boldsymbol{m}} v_h)(\boldsymbol{x}) = v_h(\boldsymbol{x} + \boldsymbol{\xi_m}) = \mathrm{e}^{\mathrm{i}\omega_h \boldsymbol{d} \cdot \boldsymbol{\xi_m}} v_h(\boldsymbol{x}) . \tag{4.10}$$

Any Bloch wave $v_h = \sum_{\boldsymbol{n}} \mathrm{e}^{\mathrm{i}\omega_h \boldsymbol{d} \cdot \boldsymbol{\xi_n}} \tau_{\boldsymbol{n}}(v_0)$ with $v_0 \in \widehat{V}_{h,\omega}$ satisfies

$$
\begin{aligned}
v_h(\boldsymbol{x} + \boldsymbol{\xi_m}) &= \sum_{\boldsymbol{n} \in \mathbb{Z}^d} \mathrm{e}^{\mathrm{i}\omega_h \boldsymbol{d} \cdot \boldsymbol{\xi_n}} v_0(\boldsymbol{x} + \boldsymbol{\xi_m} - \boldsymbol{\xi_n}) \\
&= \mathrm{e}^{\mathrm{i}\omega_h \boldsymbol{d} \cdot \boldsymbol{\xi_m}} \sum_{\boldsymbol{n} \in \mathbb{Z}^d} \mathrm{e}^{\mathrm{i}\omega_h \boldsymbol{d} \cdot \boldsymbol{\xi_{n-m}}} v_0(\boldsymbol{x} - \boldsymbol{\xi_{n-m}}) = \mathrm{e}^{\mathrm{i}\omega_h \boldsymbol{d} \cdot \boldsymbol{\xi_m}} v_h(\boldsymbol{x}) .
\end{aligned}
$$

Conversely, if $v_h = \sum_{\boldsymbol{n}} \alpha_{\boldsymbol{n}} \tau_{\boldsymbol{n}}(v_{h,\boldsymbol{n}}) \in V_{h,\omega}$ satisfies (4.10),

$$
\begin{aligned}
\sum_{\boldsymbol{n} \in \mathbb{Z}^d} \mathrm{e}^{\mathrm{i}\omega_h \boldsymbol{d} \cdot \boldsymbol{\xi_m}} \alpha_{\boldsymbol{n}} \tau_{\boldsymbol{n}}(v_{h,\boldsymbol{n}}) &= \mathrm{e}^{\mathrm{i}\omega_h \boldsymbol{d} \cdot \boldsymbol{\xi_m}} v_h = \tau_{-\boldsymbol{m}} v_h \\
&= \sum_{\boldsymbol{n} \in \mathbb{Z}^d} \alpha_{\boldsymbol{n+m}} \tau_{\boldsymbol{n}}(v_{h,\boldsymbol{n+m}}) .
\end{aligned}
$$

Since the spaces $(\tau_{\boldsymbol{n}}(\widehat{V}_{h,\omega}))_{\boldsymbol{n} \in \mathbb{Z}^d}$ have pairwise trivial intersection, the corresponding terms in the above sums must be identical. In particular, setting $v_0 = \alpha_{\boldsymbol{0}} v_{h,\boldsymbol{0}}$, the equality of the terms for $\boldsymbol{n} = \boldsymbol{0}$ implies $\alpha_{\boldsymbol{m}} v_{h,\boldsymbol{m}} = \mathrm{e}^{\mathrm{i}\omega_h \boldsymbol{d} \cdot \boldsymbol{\xi_m}} v_0$, and therefore v_h has the form (4.9).

The abstract concepts introduced above become more intuitive in the special case of a uniform discontinuous Galerkin discretization on a translation invariant mesh. Let $\mathcal{T}_h$ be a translation invariant mesh of $\mathbb{R}^d$, that is, there is a bounded submesh $\widehat{\mathcal{T}}_h \subset \mathcal{T}_h$ and a lattice $(\boldsymbol{\xi_n})_{\boldsymbol{n} \in \mathbb{Z}^d}$ such that

$$\mathcal{T}_h = \left\{ \boldsymbol{\xi_n} + \widehat{K} \ ; \ \boldsymbol{n} \in \mathbb{Z}^d, \widehat{K} \in \widehat{\mathcal{T}}_h \right\} \tag{4.11}$$

and

$$\mathbb{R}^d = \overline{\bigsqcup_{\boldsymbol{n} \in \mathbb{Z}^d, \widehat{K} \in \widehat{\mathcal{T}}_h} \boldsymbol{\xi_n} + \widehat{K}} , \tag{4.12}$$

where the union is understood to be disjoint. Leaning on the above definition, we will call $\widehat{\mathcal{T}}_h$ the *generator* of $\mathcal{T}_h$.

Let $\widehat{V}_{h,\omega} \subset L_2(\widehat{\mathcal{T}}_h)$. Because of the disjointness implied by (4.12), the spaces $(\tau_{\boldsymbol{n}}(\widehat{V}_{h,\omega}))_{\boldsymbol{n} \in \mathbb{Z}^d}$ have pairwise trivial intersection, and we can define the translation invariant space $V_{h,\omega}$ generated by $\widehat{V}_{h,\omega}$ over $(\boldsymbol{\xi_n})_{\boldsymbol{n} \in \mathbb{Z}^d}$.

Consider a function $v_{h,\boldsymbol{m}} \in \tau_{\boldsymbol{m}}(\widehat{V}_{h,\omega})$. Let $v_0 \in \widehat{V}_{h,\omega}$ such that $v_{h,\boldsymbol{m}} = \tau_{\boldsymbol{m}}(v_0)$. For any $K = \boldsymbol{\xi_n} + \widehat{K} \in \mathcal{T}_h$ and any $\boldsymbol{x} \in K$,

$$v_{h,\boldsymbol{m}}(\boldsymbol{x}) = (\tau_{\boldsymbol{m}} v_0)(\boldsymbol{x}) = v_0(\boldsymbol{x} - \boldsymbol{\xi_m}) = v_0(\boldsymbol{x} - \boldsymbol{\xi_n} - \boldsymbol{\xi_{m-n}}) .$$

If $\boldsymbol{n} = \boldsymbol{m}$, then $\boldsymbol{x} - \boldsymbol{\xi_m} \in \widehat{K}$ and $v_{h,\boldsymbol{m}}$ restricted to K is identical to the function v_0 restricted to $\widehat{K}$. If $\boldsymbol{n} \neq \boldsymbol{m}$, then $\boldsymbol{x} - \boldsymbol{\xi_m} \in \boldsymbol{\xi_{n-m}} + \widehat{K} \notin \widehat{\mathcal{T}}_h$ and $v_{h,\boldsymbol{m}}$ vanishes on K. Therefore, $\tau_{\boldsymbol{m}}(\widehat{V}_{h,\omega})$ is simply $\widehat{V}_{h,\omega}$ on the translated mesh $\boldsymbol{\xi_m} + \widehat{\mathcal{T}}_h$, and by (4.6) a general element of $V_{h,\omega}$ is a function whose restriction to any $\boldsymbol{\xi_n} + \widehat{\mathcal{T}}_h$ is, up to translation by $\boldsymbol{\xi_n}$, in $\widehat{V}_{h,\omega}$.

A similar construction is possible for other types of finite elements; however, in general the supports of the translations of $\widehat{V}_{h,\omega}$ overlap, see [7, Section 3].

---
[i]See [1, Equation (2.5)]

4.1.2 Direct measure of dispersion

Dispersion refers to the error in the phase of an approximation to a propagating wave solution of (4.1) and dissipation refers to a decrease or increase in the amplitude of the same approximation. Consider as exact solution the plane wave $u(\boldsymbol{x}) = \mathrm{e}^{\mathrm{i}\omega \boldsymbol{d} \cdot \boldsymbol{x}}$ with $\boldsymbol{d} \in S^{d-1} \subset \mathbb{R}^d$. Such a wave is periodic in direction $\boldsymbol{d}$; more precisely, for any $\boldsymbol{\xi} \in \mathbb{R}^d$,

$$(\tau_{-\boldsymbol{\xi}} u)(\boldsymbol{x}) = u(\boldsymbol{x} + \boldsymbol{\xi}) = \mathrm{e}^{\mathrm{i}\omega \boldsymbol{d} \cdot \boldsymbol{\xi}} u(\boldsymbol{x}) . \tag{4.13}$$

This property is remarkably similar to that of a Bloch wave, (4.10), which is satisfied by certain elements of the translation invariant spaces from Definition 4.3.

Dispersion and dissipation of the Galerkin method (4.2) are defined via Bloch waves that satisfy equation (4.2). The *dispersion* in direction $\boldsymbol{d}$ is $|\mathrm{Re}\,\omega_h - \omega|$ and the *dissipation* in direction $\boldsymbol{d}$ is $|\mathrm{Im}\,\omega_h - \omega| = |\mathrm{Im}\,\omega_h|$, where ω_h is the complex number closest to ω for which (4.9) is a Bloch wave solution of (4.2). This is not well defined in general, but for reasonable discretizations there is often a unique solution. Since the distinction between dispersion and dissipation is not vital for our purposes, we will study

$$|\omega_h - \omega| \tag{4.14}$$

and call this the *dispersion* of the method (4.2) in direction $\boldsymbol{d}$.

For the practical computation of dispersion, it is important to note that because of the translation invariance properties of Bloch waves and of the approximation space $V_{h,\omega}$, the problem of finding Bloch wave solutions to (4.2) can be reduced to a local problem on the generator $\widehat{V}_{h,\omega}$. Since test functions $v_h \in V_{h,\omega}^c$ are finite linear combinations of elements of $\tau_{\boldsymbol{m}}(\widehat{V}_{h,\omega})$, it suffices to satisfy (4.2) for $v_h \in \tau_{\boldsymbol{m}}(\widehat{V}_{h,\omega})$ for all $\boldsymbol{m} \in \mathbb{Z}^d$. Therefore, using (4.4) and (4.10), Bloch wave solutions are characterized by

$$0 = a_{h,\omega}(u_h, \tau_{\boldsymbol{m}} v_0) = a_{h,\omega}(\tau_{-\boldsymbol{m}} u_h, v_0) = \mathrm{e}^{\mathrm{i}\omega_h \boldsymbol{d} \cdot \boldsymbol{\xi_m}} a_{h,\omega}(u_h, v_0) \tag{4.15}$$

or equivalently,

$$a_{h,\omega}(u_h, v_0) = 0 \tag{4.16}$$

for all $v_0 \in \widehat{V}_{h,\omega}$. Inserting (4.9) leads to the variational problem for $u_0 \in \widehat{V}_{h,\omega}$,

$$\sum_{\boldsymbol{n} \in \mathbb{Z}^d} \mathrm{e}^{\mathrm{i}\omega_h \boldsymbol{d} \cdot \boldsymbol{\xi_n}} a_{h,\omega}(\tau_{\boldsymbol{n}} u_0, v_0) = 0 \qquad \text{for all} \quad v_0 \in \widehat{V}_{h,\omega} . \tag{4.17}$$

Since the elements of $\widehat{V}_{h,\omega}$ have uniformly bounded supports, finding ω_h and u_0 to satisfy (4.17) is a finite problem provided that $\widehat{V}_{h,\omega}$ is finite dimensional.

4.1.3 Indirect measure of dispersion

Although the dispersion of any method can be determined by finding the values of ω_h for which (4.17) is satisfiable, this still involves solving a complicated nonlinear problem. Further simplification is desirable.

Note that the dependence of (4.17) on ω_h is nonlinear, but the sesquilinear form $a_{h,\omega}$ defined in (4.2) depends only linearly on ω. This suggests that one

should fix ω_h and determine ω in (4.17) instead of the other way around. Assume for the moment that the spaces $V_{h,\omega} = V_h$ and $\widehat{V}_{h,\omega} = \widehat{V}_h$ are independent of ω. Then for any $\widetilde{\omega}$ let $\widetilde{\omega}_h$ be the complex number closest to $\widetilde{\omega}$ such that

$$\sum_{\boldsymbol{n} \in \mathbb{Z}^d} \mathrm{e}^{\mathrm{i}\widetilde{\omega}\boldsymbol{d}\cdot\boldsymbol{\xi_n}} \, a_{h,\widetilde{\omega}_h}(\tau_{\boldsymbol{n}} u_0, v_0) = 0 \qquad \text{for all} \quad v_0 \in \widehat{V}_h \, . \tag{4.18}$$

Intuitively, the maps $\omega \mapsto \omega_h$ and $\widetilde{\omega} \mapsto \widetilde{\omega}_h$ are inverse to each other[ii]. The advantage to computing the latter is that it involves only a linear eigenvalue problem.

In our general setting, and in particular in the case of plane wave discontinuous Galerkin methods, the test and trial space $V_{h,\omega}$ and its generator $\widehat{V}_{h,\omega}$ depend on ω. In this case, computing the inverse map to $\omega \mapsto \omega_h$ becomes more difficult since the discrete space depends on an unknown parameter[iii]. However, assuming that the difference between ω and ω_h is small, it is reasonable to solve the linear eigenvalue problem

$$\sum_{\boldsymbol{n} \in \mathbb{Z}^d} \mathrm{e}^{\mathrm{i}\widetilde{\omega}\boldsymbol{d}\cdot\boldsymbol{\xi_n}} \, a_{h,\widetilde{\omega}_h}(\tau_{\boldsymbol{n}} u_0, v_0) = 0 \qquad \text{for all} \quad v_0 \in \widehat{V}_{h,\widetilde{\omega}} \, . \tag{4.19}$$

This corresponds to finding $\widetilde{\omega}_h$ such that

$$a_h(u_h, v_h) - \widetilde{\omega}_h^2 \, (u_h, v_h)_{\mathbb{R}^d} = 0 \qquad \text{for all} \quad v_h \in V_{h,\widetilde{\omega}}^c \tag{4.20}$$

allows a '$\widetilde{\omega}$-periodic' Bloch wave solution with propagation direction $\boldsymbol{d}$. The dispersion in direction $\boldsymbol{d}$ can then be approximated by

$$|\widetilde{\omega}_h - \widetilde{\omega}| \, , \tag{4.21}$$

where $\widetilde{\omega}_h$ is chosen to be nearest to $\widetilde{\omega}$ among all complex numbers satisfying (4.20).

4.2 Dispersion in PWDG methods

4.2.1 Preliminaries

We will study the dispersion of plane wave discontinuous Galerkin methods on two-dimensional translation invariant meshes with equilateral triangles or squares as elements. Due to the regularity of the meshes and the ω-dependence of the plane wave basis functions, it suffices to consider meshes with mesh width $h = 1$[iv]. The generators of these meshes and some surrounding elements are plotted in Figure 4.1. The elements are numbered according to their generating element.

[ii]The only obstacle is the existence and uniqueness of solutions to (4.17) and (4.18).

[iii]One could solve (4.19) with $v_0 \in \widehat{V}_{h,\widetilde{\omega}_h}$ iteratively in $\widetilde{\omega}_h$ by setting $\widetilde{\omega}_h^{(0)} = \widetilde{\omega}$ and recursively determining $\widetilde{\omega}_h^{(j+1)}$ by (4.19) with $v_0 \in \widehat{V}_{h,\widetilde{\omega}_h^{(j)}}$.

[iv]In fact, the square meshes have mesh width $h = \sqrt{2}$ and edge length 1.
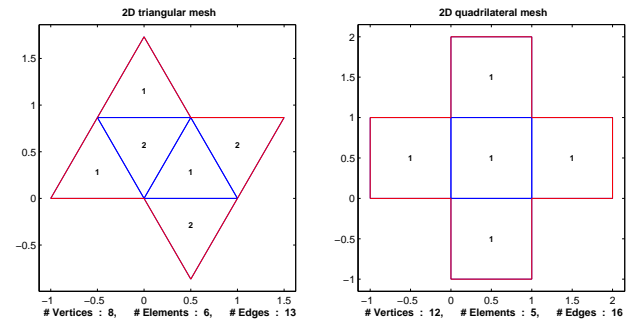
Figure 4.1: The generators of translation invariant triangular and square meshes.

4.2.2 Dependence on propagation direction

It is intuitively clear that plane wave discontinuous Galerkin methods should be best at approximating waves propagating in a direction near or at that of a plane wave basis function. In fact, it follows from the consistency of the method that there is no dispersion in the propagation directions of the basis functions since the exact plane wave solution is also a Bloch wave solution with $\omega_h = \omega$.
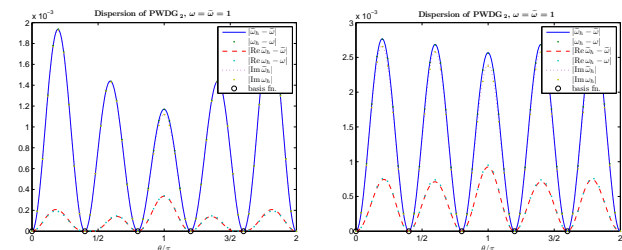

Figure 4.2: Dependence of dispersion on the propagation direction, measured by (4.21) and (4.14), for PWDG$_2$ on the triangular mesh (left) and the square mesh (right), with $\omega = \widetilde{\omega} = 1$ and using $p = 5$ local degrees of freedom.

Figure 4.2 plots the dispersion against the propagation direction

$$\boldsymbol{d} = \begin{pmatrix} \cos\theta \\ \sin\theta \end{pmatrix} \tag{4.22}$$

for PWDG$_2$ on the triangular and square translation invariant meshes. The dispersion is computed by (4.14) with $\omega = 1$ and by (4.21) with $\widetilde{\omega} = 1$. In line with the above argument, both measures of dispersion vanish in the propagation

directions of the plane wave basis functions. The two measures of dispersion are also almost identical in all other directions. Since the indirect method described in Section 4.1.3 is much more efficient than the direct approach from Section 4.1.2, we will restrict ourselves to it in the following.

4.2.3 Characterization of maximal dispersion

In this section, we will numerically study the dependence of the dispersion on $\widetilde{\omega}$ and p. In this context, the dispersion is defined as the maximum of (4.21) over all parameters other than $\widetilde{\omega}$ and p. Of coarse θ is one of these parameters; additionally, the dispersion depends on the relative orientation of the propagation directions of the basis functions as compared to the mesh. Our computations take this into account by computing the maximal dispersion over θ for several slightly rotated uniform sets of basis functions, where care is taken to avoid situations that are identical up to rotation. The dependence on the shape of the elements (triangular or square) is considered separately.
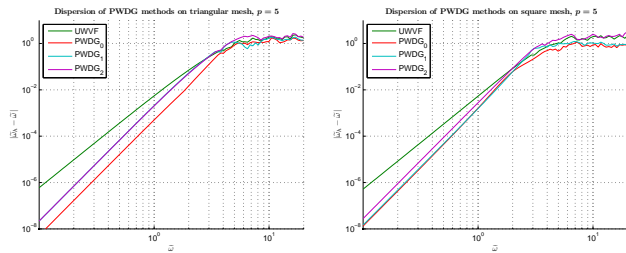
Figure 4.3: Dependence of maximal dispersion as measured by (4.21) on $\widetilde{\omega}$ for various PWDG methods on a triangular mesh (left) and a square mesh (right), using $p = 5$ local degrees of freedom.

Figure 4.3 shows the dependence of the maximal dispersion on $\widetilde{\omega}$ for $p = 5$. Apparently, dispersion decreases algebraically as $\widetilde{\omega} \to 0$. The dispersion for the PWDG_i methods is comparable, but that of UWVF seems to be slightly larger. For large $\widetilde{\omega}$, the dispersion flattens; in this area, multiple solutions of (4.20) are comparably close to $\widetilde{\omega}$ and the problem of determining the dispersion is therefore effectively ill-posed.

We would like to study the asymptotic behavior of the maximal dispersion as $\widetilde{\omega} \to 0$ more closely. To this end, we will approximate the curves in Figure 4.3 and similar by lines in bilogarithmic scale using least squares weighted by $\widetilde{\omega}^{-2}$ as described for convergence curves in Section 3.1.3. This leads to a characterization of the maximal dispersion of the form

$$|\widetilde{\omega}_h - \widetilde{\omega}| \approx c\,\widetilde{\omega}^{\eta} \qquad \text{for} \quad \widetilde{\omega} \to 0 . \tag{4.23}$$

The numerically determined values of η and c are plotted in Figure 4.4 and Figure 4.5, respectively.
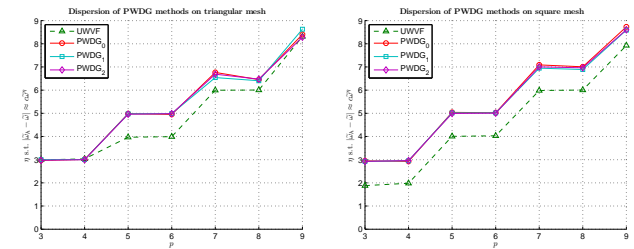
Figure 4.4: Numerically determined values of η from (4.23).
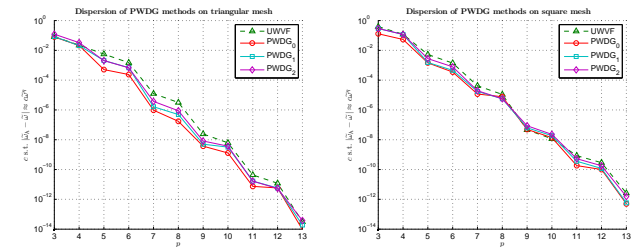
Figure 4.5: Numerically determined values of c from (4.23).

Evidently, the value of η is the same for $p = 2m$ and $p = 2m - 1$. For plane wave DG with fluxes of the form (1.35), it seems that

$$\eta = p \qquad \text{for } p \text{ odd ,} \tag{4.24a}$$
$$\eta = p - 1 \qquad \text{for } p \text{ even ,} \tag{4.24b}$$

while for the ultra-weak method on square elements

$$\eta = p - 1 \qquad \text{for } p \text{ odd ,} \tag{4.25a}$$
$$\eta = p - 2 \qquad \text{for } p \text{ even .} \tag{4.25b}$$

On triangular elements, however, the ulta-weak method has η of the form (4.24) for $p \in \{3, 4\}$ and of the form (4.25) for $p \geq 5$.

Figure 4.5 shows that c in (4.23) decreases at least exponentially in p. Again, odd p seem to be somewhat more efficient than even p, but the precise form of the dependence of c on p is unclear.

Of course, the data shown in Figure 4.4 and Figure 4.5 implies that the dispersion decreases as p increases. This is illustrated in Figure 4.6, which shows the dependence of the maximal dispersion on $\widetilde{\omega}$ for several p. The dependence on p is plotted directly in Figure 4.7. Apparently, the dispersion only begins to decrease at some, possibly large, p; it then decreases at least exponentially. This is similar to the behavior of polynomial methods, see [1, Section 3]. The different asymptotic behavior of even and odd p is only barely visible at this stage.
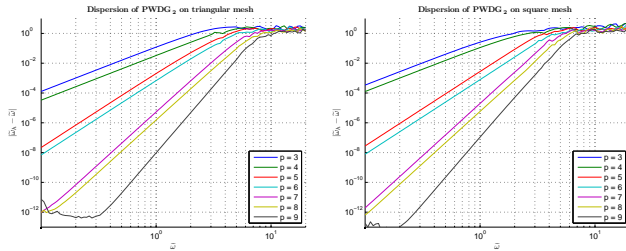
Figure 4.6: Maximal dispersion of PWDG$_2$ for various p.

Figure 4.2 above indicates that both $\omega_h - \omega$ and $\widetilde{\omega}_h - \widetilde{\omega}$ are complex[v]. The contributions of the real and imaginary parts correspond respectively to actual dispersion and dissipation. Figure 4.8 shows the relation between the maximal real part of $\widetilde{\omega}_h - \widetilde{\omega}$ and the maximal absolute value. The two are proportional for small $\widetilde{\omega}$ in the case of PWDG$_i$ methods, but the quotient seems to go to zero for UWVF. This indicates that the real part of the dispersion for UWVF may have the same asymptotic form as for PWDG$_i$[vi]. Figure 4.9 shows the relation between the maximal imaginary part of $\widetilde{\omega}_h - \widetilde{\omega}$ and the maximal absolute value; the two seem to be proportional for small $\widetilde{\omega}$.

[v]in the sense of not real

[vi]Indeed, replacing $\widetilde{\omega}_h$ for UWVF in the denominator by the corresponding value for PWDG$_2$ leads to a nonzero limit as $\widetilde{\omega} \to 0$.
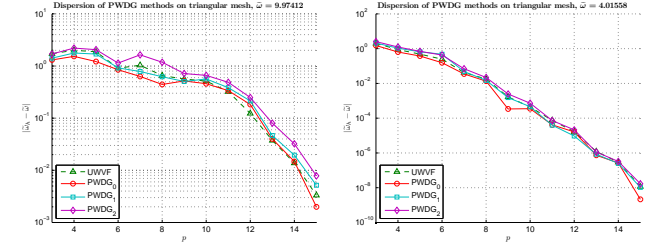
Figure 4.7: Dependence of maximal dispersion on p.
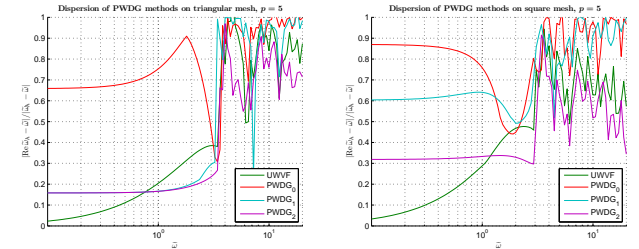
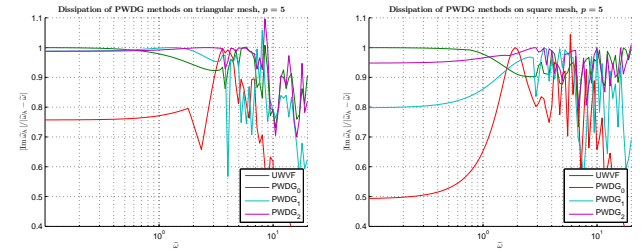Figure 4.8: Relation of maximal real part of dispersion to maximal dispersion.

Figure 4.9: Relation of maximal imaginary part of dispersion (dissipation) to maximal dispersion.

Chapter 5

The pollution effect

Dispersion and dissipation lead to errors that build up over the domain. These errors are studied experimentally and in the context of the dispersion analysis from Chapter 4.

5.1 Numerical experiments

For some problems with large wavenumbers, the asymptotic convergence behavior only sets in for very fine meshes. Figure 5.3 shows that the relative error for fixed ωh depends on ω independently of h. This ω-dependence of the convergence behavior is known as the *pollution effect*. It is responsible for the delayed convergence of the Galerkin solutions as compared to the best approximation in Figures 3.10 and 3.14.

Figure 5.2 shows the relative error of the $PWDG_2$ method with $p = 5$ for Model Problem 1 with several values of ω. The pollution effect is clearly visible; the delay in the start of convergence increases as ω increases. This is not the case for the inhomogeneous Model Problem 4, for which the analogous errors are plotted in Figure 5.1. Similar results for Model Problem 2 and its inhomogeneous counterpart are presented in [12, Section 7].

Apparently, the pollution effect strongly affects homogeneous problems[i]. It is not present in the inhomogeneous problem considered here but, by linearity, this is of course not the case for all inhomogeneous problems. The only prerequisite is a significant homogeneous solution component, for example a propagating wave.

A somewhat surprising result of the dispersion analysis is that the dispersion of UWVF for $p \in \{3, 4\}$ is worse on a square mesh than on a regular triangular mesh, as shown in Figure 4.4. This difference actually carries over to the pollution effect on unstructured triangular and quadrilateral meshes. Figures 5.4 and 5.5 show convergence curves of PWDG methods for Model Problem 1 with $p = 3$ and $\omega = 8$ on quadrilateral[ii] and triangular meshes, respectively. The convergence of UWVF on quadrilateral meshes is significantly worse than that of

---

[i] Section 5.2 demonstrates the presence of the pollution effect for propagating waves in the kernel of the Helmholtz operator

[ii] The quadrilateral meshes were generated by 'jiggling' regular tensor-product meshes.
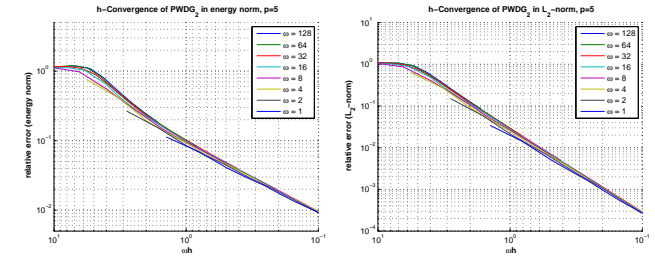
Figure 5.1: Model Problem 4: h-convergence of $PWDG_2$ for $p = 5$. The relative errors in the energy norm and the L_2-norm are plotted against ωh for various ω.
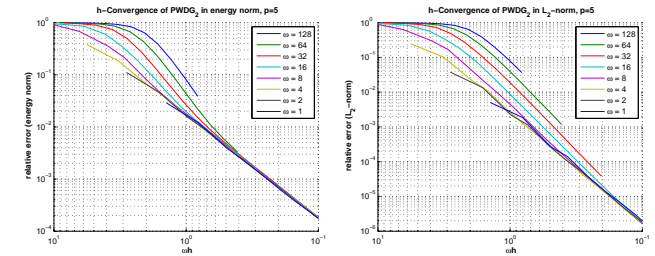

Figure 5.2: Model Problem 1: h-convergence of $PWDG_2$ for $p = 5$. The relative errors in the energy norm and the L_2-norm are plotted against ωh for various ω.
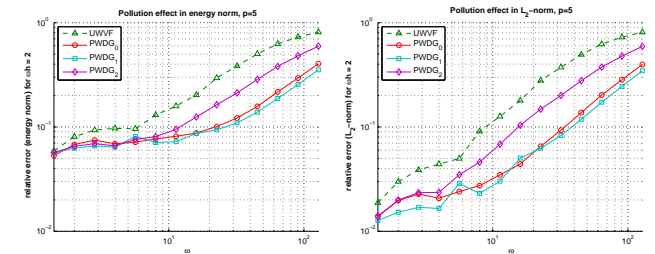

Figure 5.3: Model Problem 1: estimated relative error for fixed ωh and variable ω. Values were computed by linear interpolation (w.r.t. h) of data points in bilogarithmic scale.
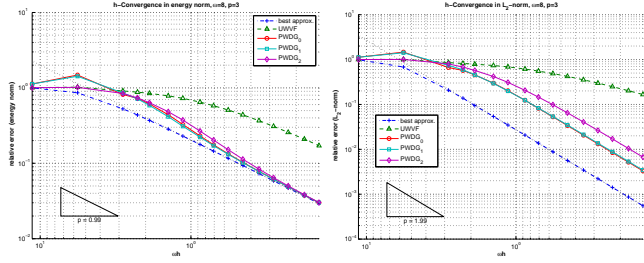
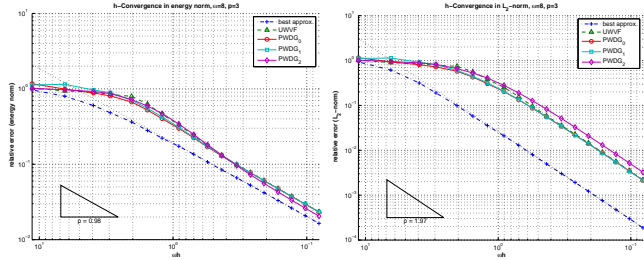Figure 5.4: Model Problem 1: h-convergence of PWDG methods for $\omega = 8$ and $p = 3$ on quadrilateral meshes.

Figure 5.5: Model Problem 1: h-convergence of PWDG methods for $\omega = 8$ and $p = 3$ on triangular meshes.

PWDG$_i$. In the L_2-norm, the convergence rate of UWVF seems to be suboptimal; this observation is completely in line with the dispersion analysis and (5.5), which predicts linear convergence. On triangular meshes, UWVF performs as well as PWDG$_i$.

5.2 Connection between dispersion and pollution

Consider a plane wave discontinuous Galerkin discretization of the (homogeneous) Helmholtz equation with wavenumber ω on a mesh with uniform element size h. This can be rescaled to have mesh width $h = 1$ and wavenumber ωh; the plane wave basis functions scale accordingly since, using the substitution $\boldsymbol{x} = h\boldsymbol{y}$,

$$\mathrm{e}^{\mathrm{i}\omega \boldsymbol{d}\cdot\boldsymbol{x}} = \mathrm{e}^{\mathrm{i}\omega h \boldsymbol{d}\cdot\boldsymbol{y}} \ .$$

Also, the numerical fluxes considered here scale properly because they only depend on the product ωh.

The dispersion analysis in Section 4.2 was restricted to meshes with element size $h = 1$. Therefore, the results are of the form

$$|\omega_h h - \omega h| \approx (\omega h)^{\eta} \tag{5.1}$$

and dividing by h leads to

$$|\omega_h - \omega| \approx \omega(\omega h)^{\eta-1} \ . \tag{5.2}$$

The following heuristic argument indicates that the pollution error behaves like $|\omega_h - \omega|$ and therefore also has the form $\omega(\omega h)^{\eta-1}$.

Consider the boundary value problem with exact solution $u(\boldsymbol{x}) = \mathrm{e}^{\mathrm{i}\omega \boldsymbol{d}\cdot\boldsymbol{x}}$ for $\omega > 0$. Dispersion analysis suggests that the discrete solution approximates $\mathrm{e}^{\mathrm{i}\omega_h \boldsymbol{d}\cdot\boldsymbol{x}}$ with $\omega_h \in \mathbb{C}$ near ω. Since

$$
\begin{aligned}
\left|\mathrm{e}^{\mathrm{i}\omega \boldsymbol{d}\cdot\boldsymbol{x}} - \mathrm{e}^{\mathrm{i}\omega_h \boldsymbol{d}\cdot\boldsymbol{x}}\right|^2 &= \left|1 - \mathrm{e}^{\mathrm{i}(\omega_h-\omega)\boldsymbol{d}\cdot\boldsymbol{x}}\right|^2 \\
&= 1 + \mathrm{e}^{-2\,\mathrm{Im}\,\omega_h \boldsymbol{d}\cdot\boldsymbol{x}} - 2\,\mathrm{Re}\!\left(\mathrm{e}^{\mathrm{i}(\omega_h-\omega)\boldsymbol{d}\cdot\boldsymbol{x}}\right) \\
&\approx 2 - 2\,\mathrm{Im}\,\omega_h \, \boldsymbol{d}\cdot\boldsymbol{x} + 2(\mathrm{Im}\,\omega_h)^2(\boldsymbol{d}\cdot\boldsymbol{x})^2 \\
&\quad - \mathrm{Re}\!\left(2 + 2\mathrm{i}(\omega_h-\omega)\boldsymbol{d}\cdot\boldsymbol{x} - (\omega_h-\omega)^2(\boldsymbol{d}\cdot\boldsymbol{x})^2\right) \\
&= \left(2(\mathrm{Im}\,\omega_h)^2 + \mathrm{Re}(\omega_h-\omega)^2\right)(\boldsymbol{d}\cdot\boldsymbol{x})^2 \ ,
\end{aligned}
$$

and assuming $|\boldsymbol{d}\cdot\boldsymbol{x}| \leq L$,

$$\left|\mathrm{e}^{\mathrm{i}\omega \boldsymbol{d}\cdot\boldsymbol{x}} - \mathrm{e}^{\mathrm{i}\omega_h \boldsymbol{d}\cdot\boldsymbol{x}}\right| \lesssim |\omega_h - \omega|\, L \lesssim \omega(\omega h)^{\eta-1} L \tag{5.3}$$

by (5.2) for small $|\omega_h - \omega|\, L$. Inserting (4.24) and (4.25), we expect a pollution error of the form

$$
\begin{aligned}
&\omega(\omega h)^{p-1} \qquad \text{for } p \text{ odd} \ , && (5.4\mathrm{a})\\
&\omega(\omega h)^{p-2} \qquad \text{for } p \text{ even} && (5.4\mathrm{b})
\end{aligned}
$$

for plane wave DG methods with fluxes of the form (1.35) and

$$\omega(\omega h)^{p-2} \qquad \text{for } p \text{ odd} , \tag{5.5a}$$

$$\omega(\omega h)^{p-3} \qquad \text{for } p \text{ even} \tag{5.5b}$$

for the ultra-weak method on square elements. On triangular elements, we expect the ultra-weak method to have a pollution error of the form (5.4) for $p \in \{3, 4\}$ and of the form (5.5) for $p \geq 5$.

Figure 4.9 indicates that dissipation is comparable to dispersion, $|\operatorname{Im} \omega_h| \approx |\omega_h - \omega| \approx \omega(\omega h)^{\eta - 1}$. Therefore, we expect a decay of the discrete solution comparable to the pollution error,

$$\left| e^{i \omega_h \boldsymbol{d} \cdot \boldsymbol{x}} \right| = e^{-\operatorname{Im} \omega_h \boldsymbol{d} \cdot \boldsymbol{x}} \approx 1 - C \omega(\omega h)^{\eta - 1} \boldsymbol{d} \cdot \boldsymbol{x} . \tag{5.6}$$

5.3 Numerical characterization of the pollution error

In the previous section, we split the error into two parts: a local error between the discrete solution and a smooth function, and the difference between this function and the exact solution. In this section, we will consider a decomposition better adapted to numerical experiments.

The total error $e_{\text{tot}} := u_h - u$ can be split into a local projection error and a remaining term, which we shall attribute to pollution. Let u_{ba} denote the best approximation of u in V_h with respect to some norm. Then

$$e_{\text{tot}} = e_{\text{poll}} + e_{\text{loc}} \tag{5.7}$$

with

$$e_{\text{poll}} := u_h - u_{\text{ba}} , \tag{5.8}$$

$$e_{\text{loc}} := u_{\text{ba}} - u . \tag{5.9}$$

Note that e_{poll} is not an ideal measure for pollution since there is always some difference between u_h and u_{ba} independent of dispersion. The convergence rates presented in Table 3.2 and elsewhere in Section 3.2 apply to the best approximation error e_{loc}. As these seem to usually reflect the asymptotic behavior of the total error e_{tot}, we expect e_{poll} to usually converge to 0 at least as fast as e_{loc}. However, since the best approximation is unaffected by pollution, the preasymptotic effects presented in Section 5.1 are caused by e_{poll} and this term is dominant on coarse meshes for large wavenumbers.

The goal of this section is to approximately determine the convergence rate of e_{poll} using the convergence data presented in Section 3.2 and Section 5.1. Values based on dispersion analysis are already given in Section 5.2. However, since the connection between dispersion analysis and actual convergence behavior is somewhat vague, it seems reasonable to confirm these values through direct computations.

We attempt to find parameters a, b and c depending on p such that the pollution error in the energy norm has the form

$$\|e_{\text{poll}}\|_\omega \approx c \omega^a (\omega h)^b . \tag{5.10}$$

However, since $\|e_{\text{poll}}\|_\omega$ is not known, we will replace it by $\|e_{\text{tot}}\|_\omega$ and restrict ourselves to points with dominant pollution error.

A typical convergence curve can be divided into three regions. Initially, there is no reduction of the error and the curve is flat or oscillatory. When convergence begins, the pollution error e_{poll} is sometimes dominant until finally asymptotic convergence sets in, which is usually determined by e_{loc}. If b is larger than the convergence rate, then we expect superasymptotic convergence in the area where the pollution error is dominant. Therefore, points on the convergence curve in a superconvergent area are likely to have dominant pollution terms and it is reasonable to assume $\|e_{\text{poll}}\|_\omega \approx \|e_{\text{tot}}\|_\omega$ in this region.

Using these points, we can determine a, b and c through linear regression, since the logarithm of (5.10) is linear in these parameters.
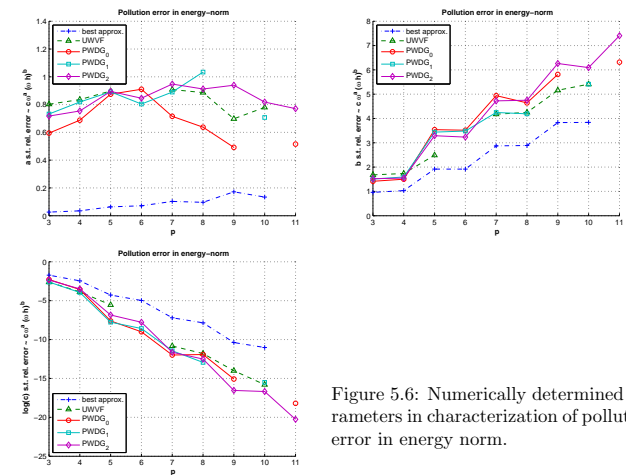

Figure 5.6: Numerically determined parameters in characterization of pollution error in energy norm.

Figure 5.3 shows values of a, b and c determined by the method described above. The linear regression is based on the data points in an area with globally maximal or almost maximal convergence rate. For comparison, parameters computed for the best approximation are also plotted. Values with a large regression error are omitted.

The first of the three plots shows the parameter a. The theoretical considerations in Section 5.2 predict $a = 1$ for the PWDG methods; of course, $a = 0$ for the best approximation. The numerically determined values of a for the PWDG methods are mostly in the interval $[0.6, 1]$, somewhat smaller than the predicted value.

The second plot shows the estimated values of b. For the best approximation, these correspond to the convergence rates given in Table 3.2. For the PWDG methods, b is somewhat smaller than the predictions (5.4) and (5.5). However, it is relatively clear that the values for $p = 2m$ and $p = 2m - 1$ are the same.

Also, the value of b for UWVF is slightly smaller than for PWDG$_i$. Both of these observations are in line with the dispersion analysis in Section 4.2.

The final plot in Figure 5.3 indicates that c decreases exponentially in p. Although the connection is not explicit in Section 5.2, this of course reflects the behavior of the corresponding parameter in the approximation of dispersion for small wavenumbers, shown in Figure 4.5.

Chapter 6

A posteriori adaptivity

Two spectral versions of PWDG are studied in this chapter. We first consider the convergence behavior for uniform bases - that is, p equidistantly spaced (on S^1) plane wave basis functions on each element - as p is increased on a fixed mesh. We then turn to an iterative method with adaptively defined plane wave basis functions, again on a fixed mesh.

6.1 p-Convergence

In this section, we consider Model Problem 2 solved on three uniform unstructured triangular meshes with 2, 24 and 125 elements, respectively. The noise in the convergence curves in the subsequent figures for large p is due to numerical instability caused by the direct use of the plane wave basis.

Figure 6.1 shows the relative errors in the energy norm and the L_2-norm for the four PWDG methods listed in Table 3.1. The convergence seems to be exponential in N. Evidently, the differences between the methods are small. Also, the plots for these two norms look virtually identical. This is not surprising since for large p, the convergence rates with respect to h are very close. Comparison of the errors of the Galerkin solutions to the best approximation errors clearly indicate a pollution effect for small p[i]. The different behavior of even and odd p observed for h-convergence in Chapters 3-5 is not apparent.

In Figure 6.2, p-convergence behavior on the three different meshes is compared. The first plot indicates that the essentially spectral method on the mesh with only two elements is significantly more efficient than the others. Of course, the total number of degrees of freedom is not an ideal measure for the computational costs since methods on coarser meshes with larger p have denser stiffness matrices. However, a comparison of the number of nonzero entries in the stiffness matrix leads to the same conclusion: 40,000 ($p = 100$), 144,648 ($p = 42$) and 317,044 ($p = 26$) are required to reach a relative error of 10^{-6} in the energy norm on the three meshes, respectively (neglecting the detail that the error doesn't quite reach this value on the middle mesh due to numerical issues).

All of the figures indicate exponential convergence in p for large enough p;

---

[i]The best approximation was only computed for small p because of numerical instability.

thus, the error can be bounded by

$$c\,e^{-a(p-p_0)}\,,\qquad p \geq p_0 \qquad\qquad (6.1)$$

for positive constants a and c. Figure 6.3, which plots the p-convergence of PWDG$_2$ for various wavenumbers ω, suggests that the convergence rate a is independent of ω and the threshold p_0 is proportional to ω. Since the best approximation error does not depend on ω independently of h, p_0 must be proportional to ωh for the best approximation. Although this seems to be in line with the second plot in Figure 6.2, it neglects the pollution evident in Figure 6.1 and (assuming a and c independent of ω and h) can therefore only carry over to the error of the Galerkin solution for sufficiently large p.
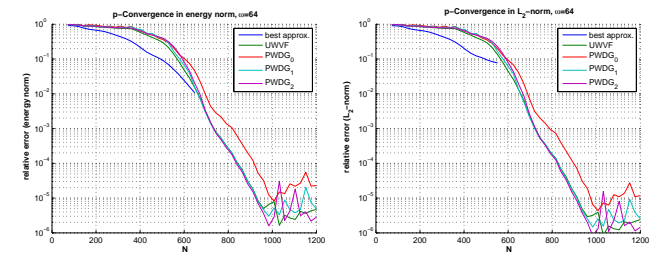

Figure 6.1: Model Problem 2: p-convergence of PWDG methods for $\omega = 64$ on mesh with 24 elements. The relative errors in the energy norm and the L_2-norm are plotted against the total number of degrees of freedom N.
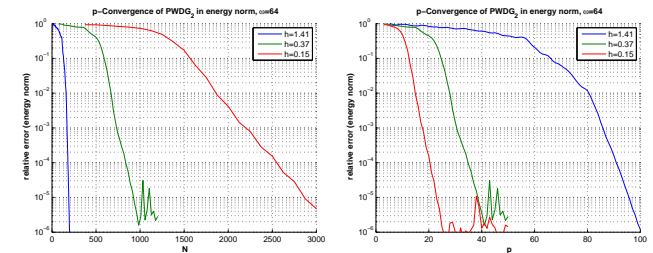

Figure 6.2: Model Problem 2: p-convergence of PWDG$_2$ for $\omega = 64$ on various meshes. The relative errors in the energy norm are plotted against the total number of degrees of freedom N and the local number of basis functions p.

6.2 Definition of new plane wave basis functions

Plane wave basis functions allow a great deal of flexibility since their propagation directions can be chosen arbitrarily. Ideally, these should be selected in such
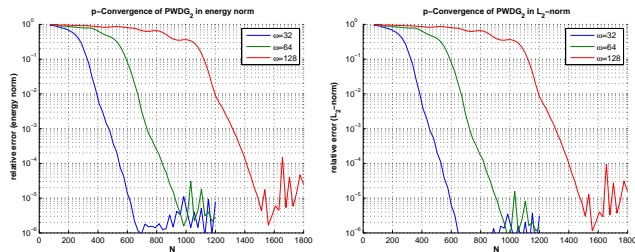
Figure 6.3: Model Problem 2: p-convergence of PWDG_2 on mesh with 24 elements for various wavenumbers. The relative errors in the energy norm and the L_2-norm are plotted against the total number of degrees of freedom N.

a way that each basis function makes a significant contribution to the exact solution.

In an iterative (a posteriori adaptive) setting, we may attempt to choose a new basis function to approximate the current error $e = u_h|_K - u|_K$ on an element $K \in \mathcal{T}_h$. This basis function is completely determined by its propagation direction.

If the error is a plane wave $e(\boldsymbol{x}) = \mathrm{e}^{\mathrm{i}\omega \boldsymbol{d}\cdot\boldsymbol{x}}$, then we can extract the propagation direction by

$$\boldsymbol{d} = \frac{\nabla e(\boldsymbol{x}_0)}{\mathrm{i}\omega e(\boldsymbol{x}_0)} \tag{6.2}$$

at any point $\boldsymbol{x}_0 \in K$. Of course, this formula is far from practical relevance since the error usually is not a plane wave; additionally, the exact error is unknown.

Let e_h be an approximation of e on K. Equation (6.2) motivates the following definition of the propagation direction $\boldsymbol{d}_h$ of a new plane wave basis function on the element K.

$$\widetilde{\boldsymbol{d}}_h := \text{Re}\, \frac{1}{|K|}\int\limits_K \frac{\nabla e_h(\boldsymbol{x})}{\mathrm{i}\omega e_h(\boldsymbol{x})}\,\mathrm{d}\boldsymbol{x}\,, \qquad \boldsymbol{d}_h := \frac{\widetilde{\boldsymbol{d}}_h}{|\widetilde{\boldsymbol{d}}_h|}\,. \tag{6.3}$$

Since the right hand side of (6.2) is not generally constant, we need to take some form of average. Also, the propagation direction must be real and of unit length, so we take the real part of this average and normalize it[ii].

Equation (6.3) can be used in an adaptive algorithm to define new basis functions given an approximation of the local error. The integral can simply be replaced by a quadrature rule. This approach should be most effective if e_h is approximately a plane wave; in this case, the integrand in (6.3) is almost constant and therefore a relatively low order quadrature rule may be sufficient.

It may be possible to find a similar formula to define a cylindrical or spherical wave as a new basis function. The case of a plane wave could then be seen as the limit for a source at infinity. Alternatively, it may be possible to drop the 'Re' in equation (6.3). Such generalizations lead to a larger class of possible basis

---
[ii]Of course, the factor $|K|^{-1}$ becomes irrelevant after normalization.

---

functions and therefore potentially to a more efficient approximation. However, no theory exists for discontinuous Galerkin methods with these basis functions and their use may lead to instabilities.

6.3   A posteriori adaptive algorithm

A vital ingredient to an a posteriori adaptive algorithm is described in Section 6.2. However, even for a given error estimator e_h, such an algorithm is far from unique. We will in this section define a (hopefully) reasonable representative for $\Omega \subset \mathbb{R}^2$; numerical experiments for it are presented in the following section.

An adaptive algorithm consists of a refinement step that adds adaptively chosen new basis functions and a thresholding step that removes superfluous degrees of freedom. Of course, the refinement step of our algorithm is based in part on (6.3). However, restriction to this formula may lead to less dominant propagation directions being overlooked. These should therefore be approximated separately, for example uniformly.

The thresholding step is also nontrivial. On a uniform mesh, the L_2-norms of the basis functions are comparable, so the coefficients of the Galerkin solution give an upper bound for the contribution of individual basis functions to the solution. However, this bound may be extremely crude and the coefficients do not provide a lower bound for arbitrary plane wave basis functions. Still, there seems to be no simple alternative to directly using the coefficients to control thresholding. The details of such a procedure are not obvious.

6.3.1   Structure of algorithm

Assume for the moment that an error estimator[iii] e_h is given. Then a precise a posteriori adaptive algorithm based on (6.3) is given by the iterative application of Algorithm 6.1[iv]. Reasonable parameters are $C_\text{T} = 4/5$, $C_\varphi = 2$ and $\varphi_0 = 2\pi/3$.

Algorithm 6.1. Parameters: $C_\text{T} \in (0,\infty)$, $C_\varphi \in (0,\infty]$, $\varphi_0 \in (0,2\pi]$, quadrature rule, fluxes $\widehat{u}_h$ and $\widehat{\boldsymbol{\sigma}}_h$.

Input: mesh $\mathcal{T}_h$, space $V_h^0 = \prod_{K\in\mathcal{T}_h} PW_\omega^{D_K^0}(K)$.

1. On each element $K \in \mathcal{T}_h$, for $p = |D_K^0|$, define

$$\varphi_\text{max} := \min\left(\frac{2\pi C_\varphi}{p}, \varphi_0\right) \tag{6.4}$$

and add basis functions such that the maximal angle between any two neighboring propagation directions is at most φ_max.[v] Let D_K^1 be the new set of propagation directions on K and V_h^1 the resulting approximation space. Furthermore, let N_φ be the total number of new basis functions.

[iii]That is, $e_h : \Omega \to \mathbb{C}$ such that $e_h \approx u_h - u$ in the interior of every element $K \in \mathcal{T}_h$.
[iv]using the space V_h as input
[v]It may also be desirable to remove basis functions that are too close together.

2. Assemble the stiffness matrix and load vector with fluxes $\widehat{u}_h$ and $\widehat{\boldsymbol{\sigma}}_h$ on V_h^1 and solve the resulting linear system. Let u_h be the Galerkin solution and e_h the approximate error.

3. For each element $K \in \mathcal{T}_h$, define $\boldsymbol{d}_K$ through (6.3). Let $N_{\boldsymbol{d}}$ be the total number of new propagation directions[vi].

4. Set $N_T = \lfloor C_T(N_{\boldsymbol{d}} + N_\varphi) \rfloor$. Let D_K^T be the set of propagation directions on $K \in \mathcal{T}_h$ corresponding to the N_T globally smallest coefficients of u_h.

5. For every $K \in \mathcal{T}_h$, define the set of propagation directions

$$D_K := (D_K^1 \backslash D_K^T) \cup \{\boldsymbol{d}_K\} .$$

The corresponding approximation space is $V_h = \prod_{K \in \mathcal{T}_h} PW_\omega^{D_K}(K)$.

Steps 1 and 2 should be repeated to compute the final solution.

The first step of Algorithm 6.1 ensures that the propagation directions of the plane wave basis functions on an element $K \in \mathcal{T}_h$ do not become too concentrated. Sometimes, Formula (6.3) may miss crucial solution components; these are approximated (more or less) uniformly through the mechanism in Step 1 as the total number of degrees of freedom on K is increased. For $C_\varphi = 2$[vii], the maximal angle between two neighboring propagation directions corresponds to the angle between $p/2$ uniformly distributed propagation directions. Therefore, the approximation of any solution component should, at worst, take twice the number of degrees of freedom as in a uniform setting. The parameter φ_0 acts as a lower bound for the number of local basis functions.

Thresholding is done in Step 4. A number of basis functions proportional to the number added in Steps 1 and 3 is removed. Let $N_0 = \dim V_h^0$ be the original number of degrees of freedom. Then there are approximately $N = N_0 + (1 - C_T)(N_{\boldsymbol{d}} + N_\varphi)$ degrees of freedom in the next iteration. Since only one new basis function per element is defined using (6.3), $N_{\boldsymbol{d}}$ is constant; N_φ can however be significantly larger. Note that the dimension of the linear system solved in Step 2 is not N_0 (or N in the next iteration), but $N_0 + N_\varphi$.

The details to Step 2 are not given. Of course, as in other adaptive algorithms, only entries of the stiffness matrix and load vector corresponding to new degrees of freedom need to be computed. Also, the resulting linear system could possibly be solved iteratively, carrying over the approximate solution of the previous iteration. For simplicity, however, we will only consider the exact discrete solution.

6.3.2 Error estimators

The ideal error estimator is the exact error, $e_h = e = u_h - u$. It has little practical relevance, but it serves to separate the effects of the error estimator from other parts of Algorithm 6.1 in numerical experiments.

An error estimator in this context does not simply gauge the size of the error; it must approximate its actual form. It seems unlikely that the error can be determined without computing a more precise solution than u_h[viii]. Therefore,

---

[vi] $N_{\boldsymbol{d}}$ is equal to the number of elements of the mesh.
[vii] A smaller value for C_φ may be better.
[viii] Of course, this more precise solution can be used as the final solution.

e_h must be based on some kind of refinement. Two forms of refinement come to mind: mesh refinement and its spectral alternative, an increase in the local number of degrees of freedom. We will consider the simplest forms of both.

The simplest mesh refinement is a single regular refinement. The elements on the refined mesh inherit the basis functions from their 'parent' on the coarse mesh. Therefore, the discrete spaces are nested and the best approximation on the fine mesh must be better than on the coarse mesh. Apart from stability issues, this also holds for the Galerkin solution. The computation of e_h simply involves evaluating the difference of the two Galerkin solutions. Note that this is in general discontinuous on elements of the coarse mesh; quadrature should therefore be done on the fine mesh. The main computational cost is solving an additional system four times the size of the original one.

The simplest spectral refinement involves doubling the number of degrees of freedom on each element, with new plane wave propagation directions defined in the middle (on S^1) of two neighboring existing ones. Again, the nesting of the two spaces ensures an improvement at least in the best approximation. The computational cost involved in evaluating e_h is the solution of an additional linear system twice the size of the original one, with four times the number of nonzero matrix entries.

We will call Algorithm 6.1 with the error estimators e_h described here 'Algorithm 6.1 with exact error', 'Algorithm 6.1 with h-refinement' and 'Algorithm 6.1 with p-refinement'.

6.4 Numerical experiments

In this section, we consider Algorithm 6.1 applied to Model Problem 2 on a uniform mesh with 24 elements[ix]. The parameters are set to $C_T = 4/5$, $C_\varphi = 2$ and $\varphi_0 = 2\pi/3$. A seven point Gauss quadrature rule of order six is used to evaluate (6.3). In all of the figures, the relative errors in the energy norm are plotted against the total number of degrees of freedom N[x] for thirty iterations of the algorithm.

The propagation directions of the basis functions generated by five iterations of Algorithm 6.1 (using the exact error as error estimator) are plotted in Figure 6.4. It should be noted that some of the coefficients of the Galerkin solution used to weight the propagation directions in the right plot are several orders of magnitude larger than the solution itself; these components of the solution cancel each other to a large extent. The connection between the values of these coefficients and the (intuitively) dominant propagation directions of the solution is therefore unclear.

The basis functions on a single element[xi] for multiple iterations of the adaptive algorithm are shown in Figure 6.5.

Figure 6.6 shows the convergence of Algorithm 6.1 (with the exact error) using the four fluxes listed in Table 3.1. For $\omega = 64$, the convergence for all of these methods is comparable; however, for the larger wavenumber $\omega = 128$, PWDG$_0$ does not seem to converge and convergence for PWDG$_1$ is delayed.

[ix] This mesh is identical to the one used for p-convergence in Section 6.1.
[x] N is the size of the linear system in Step 2 of Algorithm 6.1.
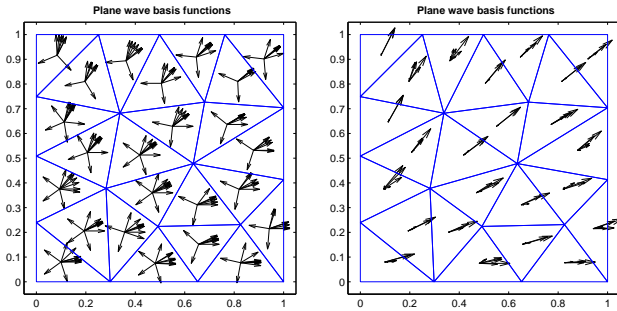[xi] the element containing the point $(\epsilon, 0.4)$

Figure 6.4: Model Problem 2: plane wave basis functions generated by five iterations of Algorithm 6.1 with exact error on mesh with 24 elements using PWDG$_2$, $\omega = 64$ and $p = 5$ initial degrees of freedom per element. On the right, the propagation directions are weighted by the absolute value of the Galerkin solution.
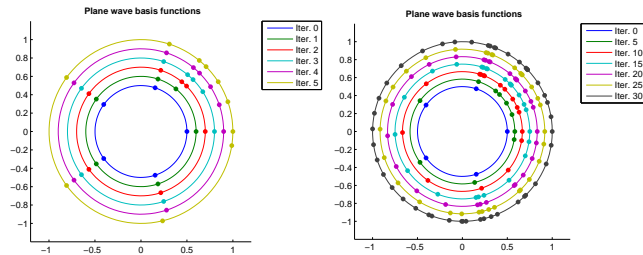

Figure 6.5: Model Problem 2: plane wave basis functions generated by Algorithm 6.1 with exact error on one element of the mesh with 24 elements using PWDG$_2$, $\omega = 64$ and $p = 5$ initial degrees of freedom per element.

The other two fluxes perform better. We will restrict ourselves to PWDG$_2$ in the following experiments.

In Figure 6.7, the convergence is plotted for various ω using $p = 5$ and $p = 11$, where in the initial discretization, $D_K = D^{p,0}$ for all $K \in \mathcal{T}_h$. In both cases, in particular for $p = 11$, the algorithm is unstable for the smallest value $\omega = 32$. For $\omega = 64$, the convergence is similar for both p. For $\omega = 128$, however, it is slightly faster with $p = 11$ than $p = 5$. For $p = 11$, the convergence for $\omega = 64$ and $\omega = 128$ is similar. This is very different from the behavior of uniform bases shown in Figure 6.3.

Figure 6.8 compares the convergence of Algorithm 6.1 with the quadrature rule used in the other experiments to a lower order and a higher order quadrature rule. All of the convergence curves flatten at least somewhat for large N and sometimes temporarily for smaller N. Higher order quadrature apparently leads to less 'premature' flattening and therefore faster initial convergence. However, the algorithm with lower order quadrature can 'catch up' and the differences between the methods appear insignificant. The better initial convergence of the method using higher order quadrature indicates that (6.3) is a good formula for defining new propagation directions since a slight change (an imprecise approximation to the integral) leads to worse convergence.

In Figure 6.9, convergence of Algorithm 6.1 is compared to uniform p-convergence. All of the computations were done on the same mesh, so the total number of degrees of freedom N is a good measure for the cost of solving the resulting linear equation. Clearly, convergence of the adaptive method sets in much earlier than that of uniform p-convergence. The initial convergence rate is similar to that of uniform bases; however, it decreases to the point that the adaptively generated discretization becomes less efficient than a uniform basis with large p.
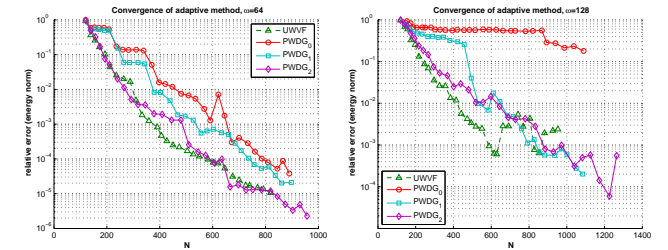

Figure 6.6: Model Problem 2: convergence of Algorithm 6.1 with exact error on mesh with 24 elements using various fluxes.

Figures 6.10 and 6.11 compare the convergence behavior of Algorithm 6.1 using the exact error to the same algorithm using h-refinement and p-refinement, respectively, as described in Section 6.3.2. For the algorithms using refinement to estimate the error, the convergence is plotted for the Galerkin solutions on both the original and refined meshes[xii]. On the original mesh, the convergence

---

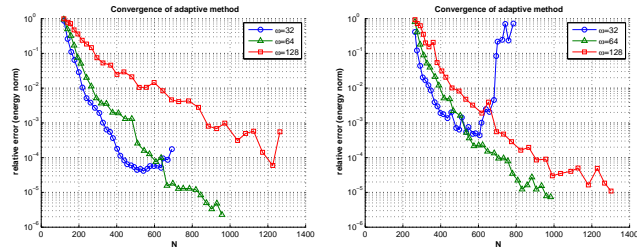[xii] The difference between these two solutions is used as an estimate for the error.

Figure 6.7: Model Problem 2: convergence of Algorithm 6.1 with exact error on mesh with 24 elements for various wavenumbers using PWDG_2 flux, starting with 5 and 11 uniform basis functions.
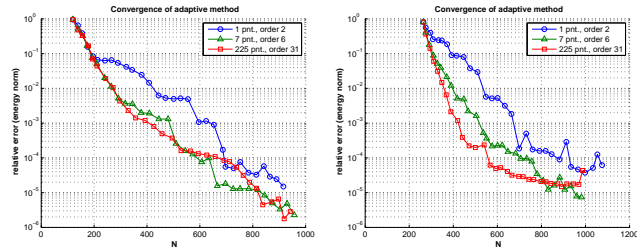

Figure 6.8: Model Problem 2: convergence of Algorithm 6.1 with exact error using three different quadrature rules. Computations were performed on mesh with 24 elements for $\omega = 64$ using PWDG_2 flux, starting with 5 and 11 uniform basis functions.
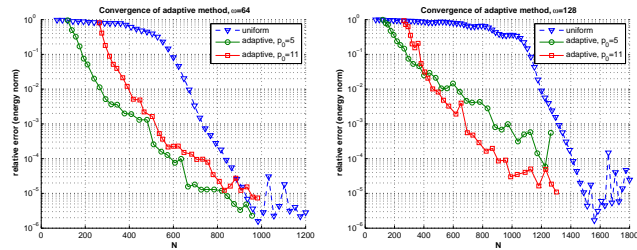

Figure 6.9: Model Problem 2: convergence of Algorithm 6.1 with exact error compared to uniform p-convergence. Computations were performed on mesh with 24 elements using PWDG_2 flux for $\omega = 64$ (left) and $\omega = 128$.
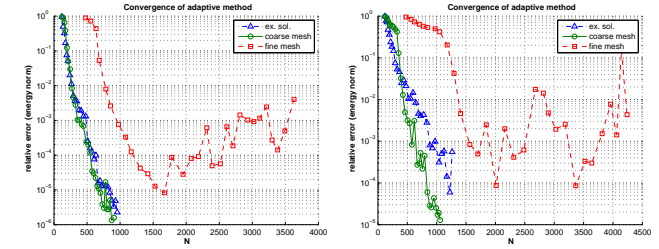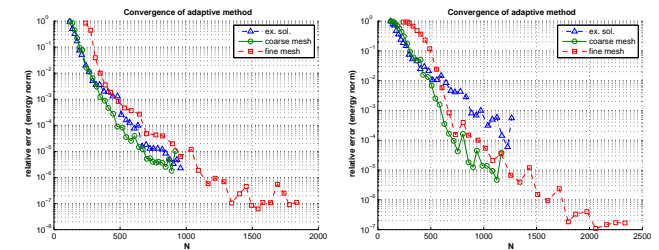
Figure 6.10: Model Problem 2: convergence of Algorithm 6.1 with h-refinement (*coarse mesh* and *fine mesh* in legend) compared to Algorithm 6.1 (*ex. sol.* in legend) with exact error. Computations were performed on mesh with 24 elements starting with 5 uniform basis functions and using PWDG_2 flux for $\omega = 64$ (left) and $\omega = 128$.

Figure 6.11: Model Problem 2: convergence of Algorithm 6.1 with p-refinement (*coarse mesh* and *fine mesh* in legend) compared to Algorithm 6.1 (*ex. sol.* in legend) with exact error. Computations were performed on mesh with 24 elements starting with 5 uniform basis functions and using PWDG_2 flux for $\omega = 64$ (left) and $\omega = 128$.

is comparable to, and sometimes better than, the method using the exact solution! This is somewhat surprising, in particular for h-refinement, which seems to reduce the error only minimally and runs into stability problems (the error on the refined mesh is larger than on the initial one). The p-refined solution, on the other hand, seems to be almost as efficient as the adaptive method itself; it always significantly reduces the error and therefore leads to a good estimate of the error. Since so much can apparently be gained by a uniform p-refinement, the parameter C_φ may have been chosen too large[(xiii)].

Compared to p-convergence with uniform bases, the convergence of Algorithm 6.1 seems to depend only minimally on the wavenumber ω; for suitably chosen parameters, convergence sets in immediately. It therefore leads to more efficient discretizations at least for large ω and relatively large error tolerances. For some reason, the convergence of Algorithm 6.1 often slows down significantly at some point. It is not clear whether this is due to numerical instability or to a deficiency in the algorithm's design. A uniform p-refinement as used in the error estimator may overcome this problem. In fact, coupling Algorithm 6.1 with p-refinement could lead to a more efficient method.

6.5 Application to acoustic scattering

In this section, uniform p-convergence and Algorithm 6.1 are studied for the more realistic Model Problem 3, which models the reflection of a plane wave on a sound-soft cylinder. All computations were done on a mesh with 100 elements, plotted in Figure 3.5 (right), using wavenumber $\omega = 16$. As above, the parameters in the adaptive algorithm are $C_T = 4/5$, $C_\varphi = 2$ and $\varphi_0 = 2\pi/3$.

The plane wave basis functions generated by five iterations of Algorithm 6.1 using the exact error as error estimator are plotted in Figures 6.12 and 6.13. The dominant basis functions correspond to the dominant propagation directions of the exact solution, plotted in Figure 3.3. In Figure 6.14, the propagation directions of the basis functions on a single element[(xiv)] are plotted for several iterations of Algorithm 6.1. They clearly accumulate in one area.

Figures 6.15, 6.16 and 6.17 show the convergence behavior of uniform p-refinement and Algorithm 6.1. The relative errors in the energy norm and the L_2-norm are plotted against the total number of degrees of freedom N. The results are similar to those presented in Sections 6.1 and 6.4 for Model Problem 2. The exponential convergence of the p-version PWDG method is confirmed. Also, the adaptive method initially converges at a rate similar to that of uniform bases, starting with significantly fewer degrees of freedom. This convergence rate eventually deteriorates. In Figure 6.16, the adaptive method is shown to be unstable for some fluxes. In the sample problem considered here, ωh is considerably smaller than in the previous example. Numerical instabilities are therefore more likely and may even be related to the early flattening in the convergence of the adaptive method.

[(xiii)] Alternatively, φ_{max} could be made to depend on the iteration or on the global number of degrees of freedom to ensure eventual approximation of all propagation directions.
[(xiv)] The element containing the point $(1.4, 0.2)$.
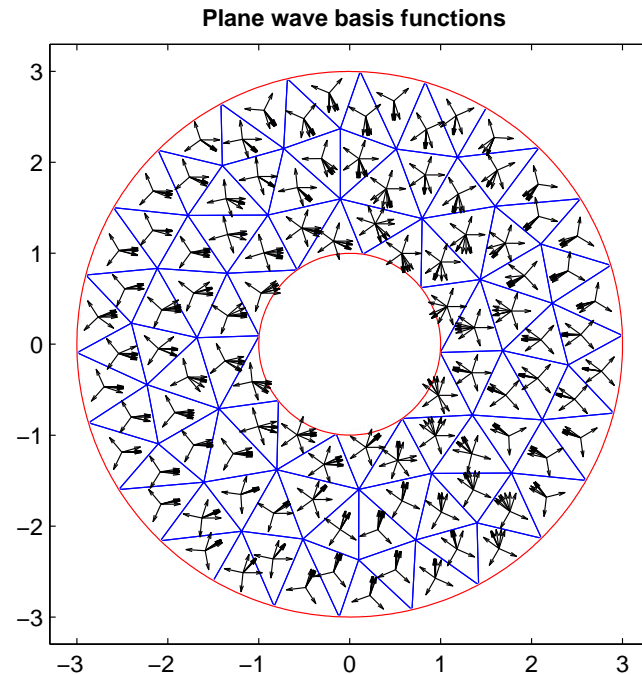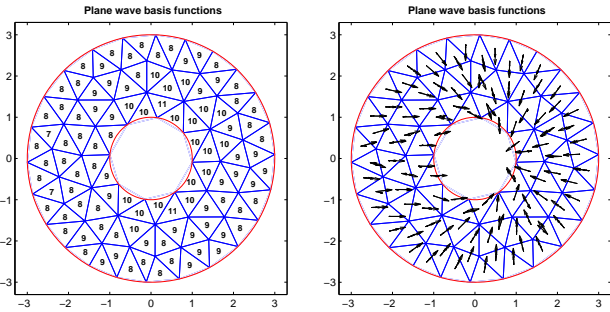

Plane wave basis functions

Figure 6.12: Model Problem 3: plane wave basis functions generated by five iterations of Algorithm 6.1 with exact error on mesh with 100 elements using PWDG$_2$, $\omega = 16$ and $p = 5$ initial degrees of freedom per element.

Figure 6.13: Model Problem 3: plane wave basis functions generated by five iterations of Algorithm 6.1 with exact error on mesh with 100 elements using $PWDG_2$, $\omega = 16$ and $p = 5$ initial degrees of freedom per element. The number of local basis functions is given in the left plot. On the right, their propagation directions are weighted by the absolute value of the Galerkin solution.
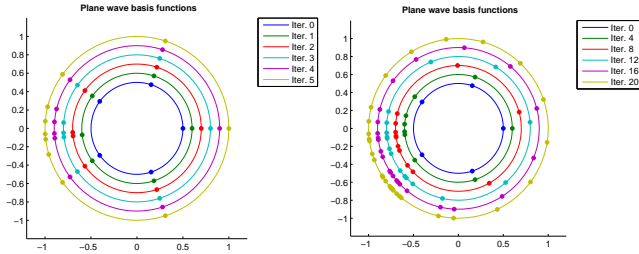

Figure 6.14: Model Problem 3: plane wave basis functions generated by Algorithm 6.1 with exact error on one element of the mesh with 100 elements using $PWDG_2$, $\omega = 16$ and $p = 5$ initial degrees of freedom per element.
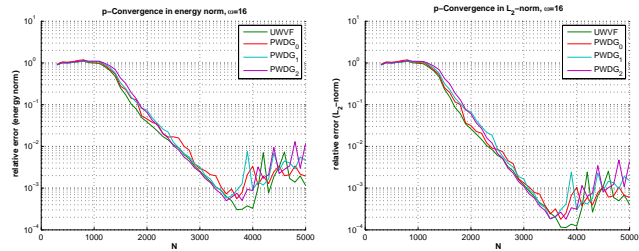

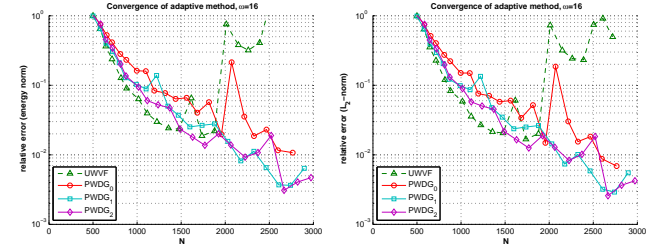Figure 6.15: Model Problem 3: p-convergence of PWDG methods for $\omega = 16$ on mesh with 100 elements.

Figure 6.16: Model Problem 3: Convergence of Algorithm 6.1 with exact error on mesh with 100 elements using various fluxes.
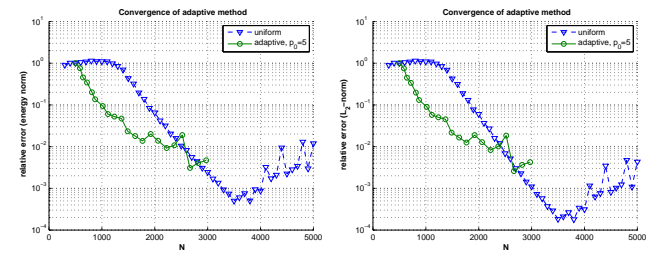

Figure 6.17: Model Problem 3: Convergence of Algorithm 6.1 with exact error compared to uniform p-convergence. Computations were performed on mesh with 100 elements using $PWDG_2$ flux for $\omega = 16$.

Chapter 7

Conclusion

Plane wave discontinuous Galerkin methods are well-suited for homogeneous Helmholtz boundary value problems. In two dimensions, the h-asymptotic convergence rate in the energy norm seems to be $\lceil \frac{p}{2} \rceil - 1$ for p plane wave basis functions per element, an essentially linear dependence on the number of local degrees of freedom. In comparison, for polynomial methods in two dimensions, the convergence rate behaves like the square root of the number of local basis functions and, accordingly, many more degrees of freedom are required to achieve the same convergence rate.[i] Experiments indicate exponential convergence in p for the spectral version of PWDG methods.

To some extent, PWDG methods are dispersive and dissipative. The resulting pollution error is apparent in both h-convergence and p-convergence experiments with large wavenumbers. However, all of these effects become minor as p is increased.

Characteristics of PWDG with odd $p = 2m-1$ and even $p = 2m$ are remarkably similar for $\omega h \to 0$.[ii] The two methods display the same h-convergence rate, and their dispersion decreases at the same rate for $\omega \to 0$. This even/odd effect is less apparent for large ωh.

Formula (6.3) can be used to define new plane wave basis functions in an a posteriori adaptive algorithm. A concept study of such a method shows initial exponential convergence, but subsequent flattening. The initial convergence rate is similar to that of p-convergence with uniform bases; however, the dependence on the wavenumber ω is significantly smaller. For large ω, the adaptive algorithm displays an earlier onset of convergence than uniform bases and therefore leads to more efficient discretizations. A further improved algorithm may maintain the initial convergence rate and make (6.3) practically applicable.

---

[i]For polynomial tensor product DG methods, $(\gamma + 1)^2$ degrees of freedom per element are required to achieve convergence rate γ, compared to $2\gamma + 1$ for PWDG.

[ii]One exception is the constant C_{tinv} plotted in Figure 1.1, which is similar for $p = 2m+1$ and $p = 2m$.

Bibliography

[1] M. Ainsworth. Discrete dispersion relation for hp-version finite element appriximation at high wave number. *SIAM J. Numer. Anal.*, 42(2):553–575, 2003.

[2] D. N. Arnold, F. Brezzi, B. Cockburn, and L. D. Marini. Unified analysis of discontinuous Galerkin methods for elliptic problems. *SIAM J. Numer. Anal.*, 39(5):1749–1779, 2002.

[3] I. Babuška and J. Melenk. The partition of unity method. *Int. J. Numer. Methods Eng.*, 40(4):727–758, 1997.

[4] A. Buffa and P. Monk. Error estimates for the ultra weak variational formulation of the Helmholtz equation. *Math. Mod. Numer. Anal.*, 2007. Submitted.

[5] O. Cessenat and B. Després. Application of an ultra weak variational formulation of elliptic PDEs to the two-dimensional Helmholtz problem. *SIAM J. Numer. Anal.*, 35(1):255–299, February 1998.

[6] O. Cessenat and B. Després. Using plane waves as base functions for solving time harmonic equations with the ultra weak variational formulation. *J. Computational Acoustics*, 11:227–238, 2003.

[7] A. Deraemaeker, I. Babuška, and P. Bouillard. Dispersion and pollution of the FEM solution for the Helmholtz equation in one, two and three dimensions. *Int. J. Numer. Meth. Engng.*, 46:471–499, 1999.

[8] B. Després. Sur une formulation variationelle de type ultra-faible. *C.R. Acad. Sci. Paris, Ser. I*, 318:939–944, 1994.

[9] C. Farhat, I. Harari, and U. Hetmaniuk. A discontinuous galerkin method with lagrange multipliers for the solution of helmholtz problems in the mid-frequency regime. *Computer Methods in Applied Mechanics and Engineering*, 192(11):1389–1419, 2003.

[10] C. Farhat, R. Tezaur, and P. Weidemann-Goiran. Higher-order extensions of a discontinuous Galerkin method for mod-frequency Helmholtz problems. *Int. J. Numer. Meth. Engng.*, 61:1938–1956, 2004.

[11] E. Giladi and J. B. Keller. A hybrid numerical asymptotic method for scattering problems. *Journal of Computational Physics*, 174:226–247, 2001.

[12] C. J. Gittelson, R. Hiptmair, and I. Perugia. Plane wave discontinuous Galerkin methods. Preprint NI07088-HOP, Isaac Newton Institute Cambridge, Cambridge, UK, December 2007. http://www.newton.cam.ac.uk/preprints/NI07088.pdf.

[13] R. Hiptmair and P. Ledger. A quadrilateral edge element scheme with minimum dispersion. Report 2003-17, SAM, ETH Zürich, Zürich, Switzerland, December 2003.

[14] T. Huttunen, P. Monk, and J. P. Kaipio. Computational aspects of the ultra-weak variational formulation. *Journal of Computational Physics*, 182:27–46, 2002.

[15] F. Ihlenburg. *Finite element analyises of acoustic scattering*, volume 132 of *Applied Mathematical Sciences*. Springer-Verlag New York, 1998.

[16] O. Laghrouche, P. Bettess, and R. J. Astley. Modelling of short wave diffraction problems using approximating systems of plane waves. *Int. J. Numer. Meth. Engng.*, 54:1501–1533, 2002.

[17] J. Melenk. *On Generalized Finite Element Methods.* PhD thesis, University of Maryland, USA, 1995.

[18] P. Monk and D. Wang. A least squares method for the helmholtz equation. *Computer Methods in Applied Mechanics and Engineering*, 175:121–136, 1999.

[19] A. A. Oberau and P. M. Pinsky. A multiscale finite element method for the Helmholtz equation. *Comput. Methods Appl. Mech. Engrg.*, 154:281–297, 1998.

[20] E. Perrey-Debain, O. Laghrouche, and P. Bettess. Plane-wave basis finite elements and boundary elements for three-dimensional wave scattering. *Phil. Trans. R. Soc. London A*, 362(1816):561–577, 2004.

[21] M. Stojek. Least-squares Trefftz-type elements for the Helmholtz equation. *Int. J. Numer. Meth. Engr.*, 41(5):831–849, 1998.

[22] S. Suleau, A. Deraemaeker, and P. Bouillard. Dispersion and pollution of meshless solutions for the Helmholtz equation. *Comput. Methods Appl. Mech. Engrg.*, 190:639–657, 2000.

[23] R. Tezaur and C. Farhat. Three-dimensional discontinuous Galerkin elements with plane waves and lagrange multipliers for the solution of mid-frequency helmholtz problems. *Int. J. Numer. Meth. Engr.*, 66(5):796–815, 2006.

[24] L. L. Thompson. A review of finite-element methods for time-harmonic acoustics. *J. Acoust. Soc. Am.*, 119(3):1315–1330, March 2006.

[25] L. L. Thompson and P. M. Pinsky. A Galerkin least squares finite element method for the two-dimensional Helmholtz equation. *Int. J. Numer. Meth. Engng.*, 38:371–397, 1995.